

# 1 Neutron-Neutron Correlations in the Photofission of U-238

2 J. Burggraf, D.S. Dale, and T. Forest  
3

4      *Department of Physics,*  
5      *Idaho State University, Pocatello, ID 83201*

6 G. Warren, S. Stave, S. Behling, and E. Church  
7

8      *Pacific Northwest National Laboratory, PO Box 999, Richland, Washington 99352*

(Dated: October 4, 2019)

9 **Background:** In the fission of actinides, the nearly back-to-back motion of the fission fragments has a strong  
10 effect on the kinematics of fission neutrons. This leads to a favoring of opening angles near  $0^\circ$  and  $180^\circ$  in the  
11 neutron-neutron (n-n) opening angle distribution of correlated neutron pairs from the same fission event.

12 **Purpose:** To measure the n-n opening angle and energy correlations in the photofission of  $^{238}\text{U}$ . As of this  
13 writing, measurements of correlated n-n opening angle distributions have been reported only for the spontaneous  
14 and neutron-induced fission of actinides. This work is the first to report such a measurement using photofission  
15 and will provide useful experimental input for photofission models used in codes such as MCNP and FREYA.

16 **Method:** Fission is induced using bremsstrahlung photons produced via a low duty factor, pulsed, linear electron  
17 accelerator. The bremsstrahlung photon beam impinges upon a  $^{238}\text{U}$  target that is surrounded by a large neutron  
18 scintillation detection system capable of measuring particle position and time of flight, from which n-n opening  
19 angle and energy are measured. Neutron-neutron angular correlations are determined by taking the ratio between  
20 a correlated n-n distribution and an uncorrelated n-n distribution formed by the pairing of neutrons produced  
21 during different beam pulses. This analysis technique greatly diminishes effects due to detector efficiencies,  
22 acceptance, and experimental drifts.

23 **Results:** The angular correlation of neutrons from the photofission of  $^{238}\text{U}$  shows a high dependence on neutron  
24 energy as well as a dependence on the angle of the emitted neutrons with respect to the incoming photon beam.  
25 Angular correlations were also measured using neutrons from the spontaneous fission of  $^{252}\text{Cf}$ , showing good  
26 agreement with past measurements.

27 **Conclusions:** The measured angular correlations reflect the underlying back-to-back nature of the fission fragments.  
28 An anomalous decline in n-n yield was observed for opening angles near  $180^\circ$  for  $^{238}\text{U}$ .

## 29 CONTENTS

30 I. Overview of Neutron-Neutron Angular  
31 Correlations in Fission  
32    A. Theoretical Basis  
33    B. Past Measurements: Spontaneous and  
34       Neutron Induced Fission  
35    C. Considerations for Photofission

36 II. Experimental Setup  
37    A. Detectors  
38    B. Detector Shielding  
39    C. Bremsstrahlung Photon Beam  
40    D. DU Target  
41    E. Electronics

42 III. Measurement Techniques  
43    A. Particle Time of Flight and Energy  
44       Determination  
45    B. Particle Position Reconstruction  
46    C. Measurements with  $^{252}\text{Cf}$

47 IV. Analysis  
48    A. Cancelation of Detector Efficiencies, Drifts,  
49       and Geometric Phase Space  
50    B. Subtraction of Accidental Coincidences

## 51 V. Potential sources of error

52    A. Correlated versus uncorrelated n-n energy  
53       distribution  
54    B. Detector Cross-talk  
55       1. Simulation of Detector Cross-talk  
56       C. Neutron Scattering within the Target

## 57 VI. Results

58    A. Comparisons with FREYA  
59    B. Anomalous emission at large opening  
60       angles  
61       C. Considering  $\theta_{abs}$

## 62 VII. Concluding Remarks

## 63 VIII. Acknowledgments

## 64 References

## 65 I. OVERVIEW OF NEUTRON-NEUTRON 66 ANGULAR CORRELATIONS IN FISSION

67 The fission process is characterized by the emission of  
68 neutrons. Neutron emission in fission can be classified  
69 into two categories depending on the time of emission:

70 delayed and prompt. Prompt fission neutrons are de-  
 71 fined as neutrons that are emitted either immediately  
 72 after ( $< 10^{-14}$  seconds) fission, or during the scission  
 73 of the nucleus, and account for  $\sim 99\%$  of neutron emis-  
 74 sion [1]. Delayed neutrons are not relevant to the present  
 75 work because they account for only  $\sim 1\%$  of total neutron  
 76 emission in actinide photofission [1], and they are emit-  
 77 ted milliseconds to minutes after fission which is well out-  
 78 side the neutron acceptance timing window of the present  
 79 work.

80 Prompt fission neutron production occurs by means of  
 81 two distinct mechanisms. The dominant mechanism is  
 82 neutron emission from the fully accelerated fragments.  
 83 The second mechanism, referred to as *early* or *scission*  
 84 neutron emission, is the emission of neutrons during ei-  
 85 ther the scission of the nucleus or the acceleration of the  
 86 fission fragments. A large number of past studies have  
 87 established that the majority of prompt fission neutrons  
 88 (80%–98%) are emitted from the fully accelerated frag-  
 89 ments, while scission neutrons account for the remaining  
 90 2%–20% percent [2]. The nature of scission neutrons has  
 91 remained elusive since their first tentative observation in  
 92 1962 by Bowman *et al.* [3].

### A. Theoretical Basis

94 The neutron-neutron (n-n) opening angle distribution  
 95 of correlated neutron pairs, as seen in the lab frame, is  
 96 widely used for the quantification of n-n angular correla-  
 97 tions. Angular correlations in fission neutrons arise due  
 98 to the kinematics of the fission fragments. It has been  
 99 shown that neutrons released from the fully accelerated  
 100 fission fragments are evaporated isotropically in the frag-  
 101 ment's rest frame, and are emitted at speeds compara-  
 102 ble to that of the fragments themselves [4]. This leads  
 103 to the well-known U-shaped distribution in neutron-  
 104 neutron opening angle ( $\theta_{nn}$ ), which has been reported  
 105 in studies of neutron-induced, spontaneous, and in this  
 106 work, photofission.

107 The U-shaped distribution of  $\theta_{nn}$  can be understood  
 108 as the result of the boost provided to the neutrons by the  
 109 fission fragments in binary fission. Due to the conserva-  
 110 tion of momentum, the fully accelerated fission fragments  
 111 are traveling nearly back-to-back, and neutrons emitted  
 112 from different fragments are boosted in opposite direc-  
 113 tions, whereas neutrons emitted from the same fragment  
 114 are boosted in the same direction. Thus, because the  
 115 velocities of the fission fragments are large enough to ac-  
 116 count for a significant portion of the kinetic energy of  
 117 fission neutrons, neutron pairs emitted from the acceler-  
 118 ated fragments exhibit a favoring of opening angles near  
 119 0° if emitted from the same fragment and 180° if emit-  
 120 ted from different fragments, and consequently, result in  
 121 a suppression of opening angles near 90°.

122 The favoring of large and small n-n opening angles  
 123 shows a strong dependence on neutron energy. Neutrons  
 124 with higher energy are more likely to have been emit-

125 ted along the same direction as the fission fragments and  
 126 are therefore expected to favor large and small opening  
 127 angles. On the other hand, neutrons emitted with lower  
 128 energy are more susceptible to kinematical focusing along  
 129 the direction of the recoil of the emitting fragment. The  
 130  $\theta_{nn}$  distribution and its dependence on neutron energy  
 131 are expected to shed light on several fundamental aspects  
 132 of the fission process including the neutron multiplicity  
 133 distributions associated with the light and heavy fission  
 134 fragments, the nuclear temperatures of the fission frag-  
 135 ments, and the mass distribution of the fission fragments  
 136 as a function of energy released. In addition, the unique  
 137 kinematics of fission and the resulting n-n correlations  
 138 have the potential to be the basis for a new tool to char-  
 139 acterize fissionable materials [5].

### B. Past Measurements: Spontaneous and Neutron Induced Fission

142 The first measurement of the angular correlation  
 143 among coincident neutrons from fission was performed  
 144 by Debenedetti *et al.* [6] in 1948 from neutron induced  
 145 fission of  $^{235}\text{U}$ . The next measurement of this type was  
 146 performed by Pringle and Brooks in 1975 [7], in which  
 147 neutrons emitted from the spontaneous fission (SF) of  
 148  $^{252}\text{Cf}$  were found to have high coincidence rates at small  
 149 opening angles near 0° and large opening angles near  
 150 180°. In order to produce a result that is insensitive to  
 151 the effects of detector geometry and efficiency, the present  
 152 work uses techniques similar to those used in reference [7],  
 153 in which a ratio is taken between a correlated opening an-  
 154 gle distribution and an uncorrelated opening angle distri-  
 155 bution. Measurements of n-n angular correlation in the  
 156 SF of  $^{252}\text{Cf}$ , the most studied case of correlated neutron  
 157 emission in fission (see Refs. [7–10]), were also performed  
 158 in the present work and show good agreement with past  
 159 measurements, as seen in Fig. 1. Correlated n-n measure-  
 160 ments have also been performed using thermal neutron  
 161 induced fission of  $^{235}\text{U}$ ,  $^{233}\text{U}$ , and  $^{239}\text{Pu}$  [11], as well as  
 162 the SF of  $^{240}\text{Pu}$  [12].

### C. Considerations for Photofission

164 The photofission reaction occurs during the de-  
 165 excitation of a nucleus after the absorption of a pho-  
 166 ton. For photon energies between 6 and 25 MeV, this  
 167 absorption occurs primarily via the giant dipole reso-  
 168 nance (GDR) excitation. One distinct and useful as-  
 169 pect of photofission, relative to neutron-induced fission,  
 170 is the low transfer of angular momentum to the nucleus,  
 171 which gives rise to a simpler set of selection rules for  
 172 the transfer of angular momentum. For the photofis-  
 173 sion of even-even nuclei, excitation occurs primarily via  
 174 electric dipole transitions, and to a lesser extent electric  
 175 quadrupole transitions, which gives rise to anisotropies  
 176 in the fission fragment angular distributions that are far

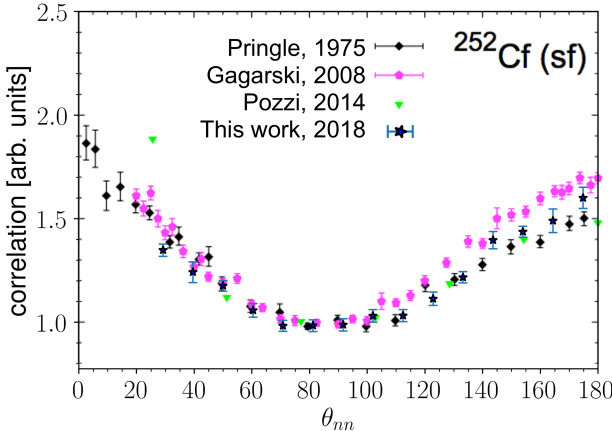


**FIG. 1:**  $\theta_{nn}$  distribution from the spontaneous fission of  $^{252}\text{Cf}$ . The minimum neutron energy cut-off for Pringle [7], Gagarski [9], and Pozzi [12] is 0.425 MeV, 0.425 MeV, and 0.7 MeV, respectively, and for this work is 0.4 MeV.

more pronounced than for other types of fission [13, 14].  
 These anisotropies are expressed in the angular distribution of emitted neutrons. For these reasons, photofission is increasingly being used as a means to study sub-nuclear structures and the fundamentals of the fission process. Such studies are needed in order to dial in various model parameters required for an accurate theoretical description of the fission process.

## II. EXPERIMENTAL SETUP

This experiment was carried out at the Idaho Accelerator Center (IAC), using their short-pulsed linear accelerator, which is an L-band frequency (1300 MHz) electron linear accelerator. See section II C for the accelerator parameters used during the experiment. Figure 2 shows a top-down diagram of the experimental arrangement.

### A. Detectors

The detection system measures neutron position and time of flight (ToF), which is defined as the time taken for a particle to travel from the fission target to a detector. The purpose of the ToF measurement is to determine the kinetic energy of detected neutrons and to distinguish between photons and neutrons. The detection system's positional precision is  $\pm 9$  cm, which gives an average angular precision of  $\pm 6^\circ$  in opening angle reconstruction for a target to detector distance of 1.25 m.

The detection system consists of fourteen shielded scintillators made from Polyvinyl Toluene (PVT) arranged in a ring around the target (see Figs. 2 and 3). Attached to both ends of each scintillator are 10-cm long, non-scintillating, ultra-violet transmitting, plastic light-guides. A Hamamatsu 580-17 photomultiplier (PMT)

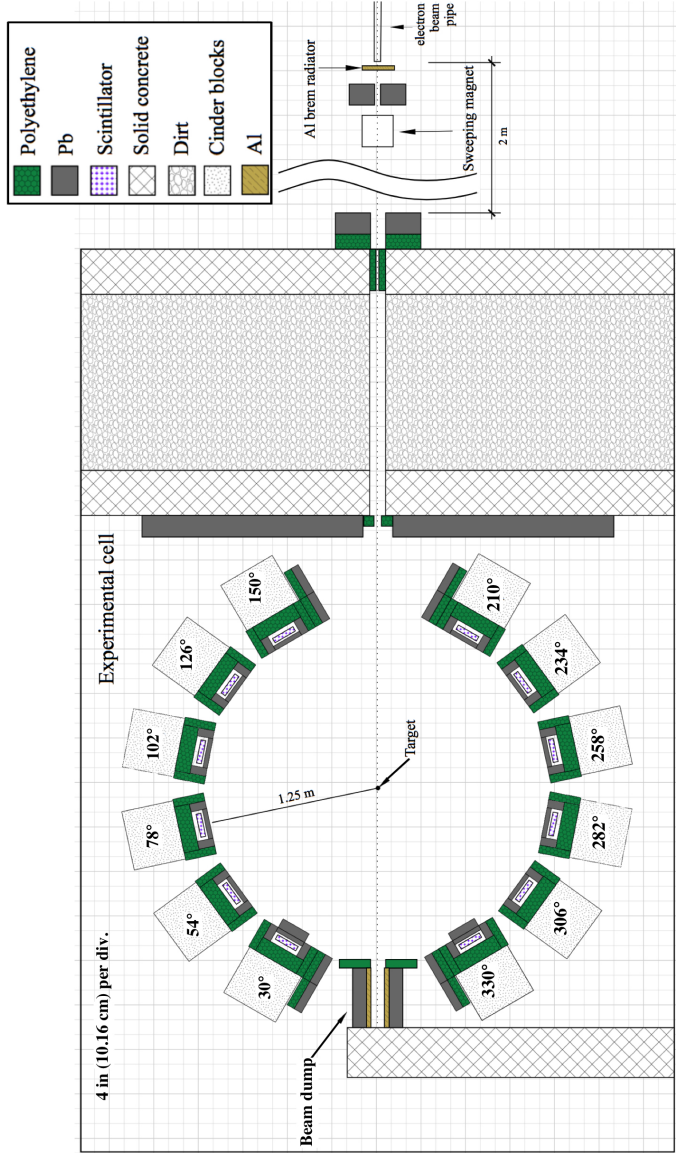


**FIG. 2:** To-scale, top down diagram of the experimental setup. An electron beam impinges upon a 3.8 cm thick Al radiator, and the resulting bremsstrahlung beam enters the experimental cell from the top of the figure. The supporting structure for each detector has been labeled according to the angle, in degrees, between the center of each detector and direction of the incoming photon beam. The fission target, a  $0.05 \times 2 \times 4 \text{ cm}^3$   $^{238}\text{U}$  cuboid, is rotated slowly about the vertical axis in order to mimic the effect of using a cylindrical target.

tube is fixed to each light-guide using optical glue. In order to increase the chance that scintillation light remains inside the scintillator, the scintillators were polished to remove micro-imperfections and were then wrapped in reflective aluminized mylar.

Ten out of the fourteen scintillators had dimensions of  $76.2 \times 15.2 \times 3.8 \text{ cm}^3$ . The remaining four, the forward-most detectors located at  $\pm 30^\circ$  with respect to the beam,

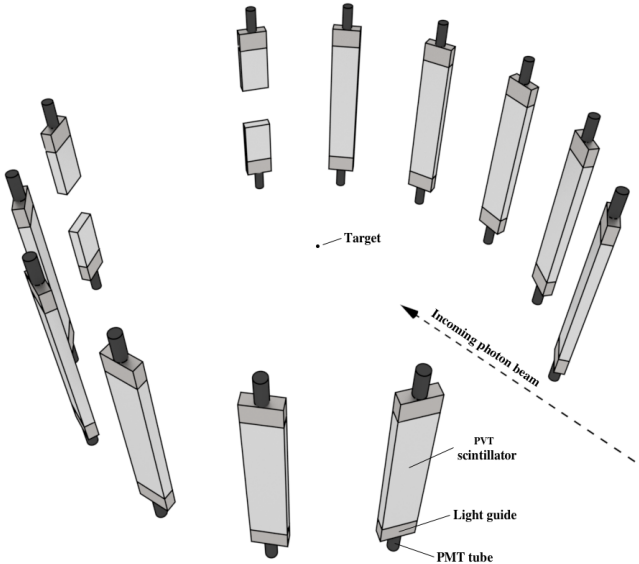


**FIG. 3:** 3-D rendering of the bare, unshielded scintillators, along with PMTs and light guides. Most of the open space between the scintillators was occupied by shielding, as seen in Fig. 2.

had dimensions of  $25.4 \times 15.2 \times 3.8 \text{ cm}^3$ . These scintillators, 1/3 the length of the rest, are the result of the segmentation of two normally sized scintillators in order to address the high photon flux at these locations caused by the forward scattering of photons from the target. Prior to segmentation, a photon was registered in the forward-most detectors at a rate of about 0.9 photons per pulse, and because the electronics were operated in single hit mode (see section II E), this greatly reduced the effective neutron detection efficiency. After segmentation and optimization of shielding, the photon detection rate was about 0.2 photons per pulse in each segmented detector. The segmented detectors also differ from the rest in that they were instrumented with only a single PMT, and therefore provide a comparatively lower precision in energy and position measurements. In order to test for systematic errors that may have resulted from the use of the segmented detectors, opening angle measurements were compared with and without their use, and the differences were well within experimental errors.

The relative efficiencies of the neutron detectors as a function of neutron energy and detector location were calculated by dividing the measured by the known yields of neutrons from the SF of  $^{252}\text{Cf}$ . The results are shown in Fig. 4. Note that the effects of the uncertainty in measured neutron energy (seen in Fig. 10) are folded into this calculation. The analysis techniques described in section IV are designed to eliminate the effects of detector efficiency from the final result.

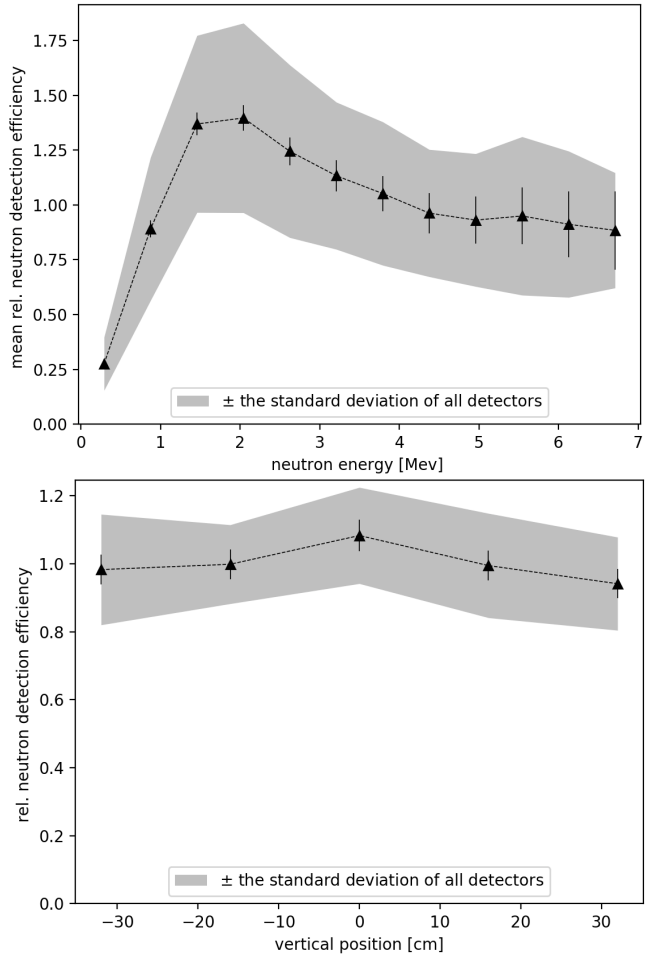
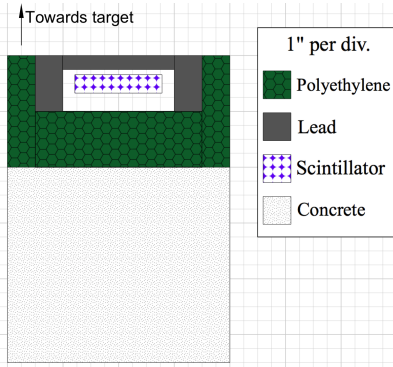


**FIG. 4:** (top) The mean relative neutron detection efficiency of all detectors as a function of neutron energy is calculated by dividing the measured energy distribution by the known energy distribution of neutrons from the SF of  $^{252}\text{Cf}$ . The relative efficiency differs from detector to detector, as demonstrated by the shaded region, which corresponds to the standard deviation of the relative efficiencies of all detectors. The error bars represent the uncertainty in the mean. (bot) Mean relative neutron detection efficiency as a function of the reconstructed position along the detectors longest axis.

## B. Detector Shielding

The detector shielding, depicted in Fig. 5, was constructed using lead and polyethylene with the aim of reducing detector cross-talk, the detection of photons, and noise. The sides of each scintillator were shielded with 5 cm of lead followed by 5 cm of polyethylene to reduce the chance of neutron cross-talk. Lead was not placed behind the scintillators after an MCNP-POLIMI simulation indicated that cross-talk would occur at significant rates otherwise. Instead, 10 cm of polyethylene was placed behind the scintillators. For a detailed discussion about the issue of cross-talk, see section V B.

The front face of each detector was subject to



334 the target would see relatively fewer neutrons due to increased scattering along this axis. This bias is removed  
 335 by slowly rotating the target about the vertical axis during data acquisition at a rate of one rotation per 8 seconds.  
 336  
 337

339

### E. Electronics

340 A data acquisition system based on the NIM/VME standard was used. A schematic of the data acquisition logic is shown in Figure 7. The PMTs are supplied negative voltages ranging from 1300 to 1500 V by a LeCroy 341 1458 high voltage mainframe. Analog signals from the 342 PMTs were fed into a leading edge discriminator (CAEN 343 Mod. N841) with input thresholds ranging from 30 mV 344 to 50 mV. The threshold and supply voltages were determined 345 individually for each detector to minimize noise, 346 while simultaneously matching the efficiencies of all the 347 detectors as closely as possible. Logic signals from the 348 discriminator were converted to ECL logic and fed into a 349 CAEN model V1290A TDC. The timing of signals from 350 the PMTs were always measured relative to a signal from 351 the accelerator provided at the beginning of each pulse. 352 Even though a multi-hit TDC was used, only the first 353 signal in each pulse from any given PMT was taken into 354 account due to concerns over dead-time within the electronics 355 and signal reflections within the cables. On the 356 software side, the CODA 2.5 [15] software package developed 357 by Jefferson Laboratory was used to read out the 358 data from the TDC and digitally store it for analysis.  
 359  
 360

362

## III. MEASUREMENT TECHNIQUES

363  
 364

### A. Particle Time of Flight and Energy Determination

365 The ToF of detected particles is used to distinguish 366 between neutrons and photons and to determine neutron 367 energy. A particle's reconstructed position is used to 368 determine direction of motion, which is then used to calculate 369 the opening angle between pairs of detected particles.  
 370 Position and ToF are each determined using the timing 371 of coincident signals from both PMTs of a given detector.

372 The sum of the times required for scintillation light 373 to travel from the point of scintillation to both PMTs 374 is equal to the time required for the light to travel the 375 full length of the scintillator, which is a constant for light 376 that travels parallel to the length of the scintillator. This 377 is supported by data, shown in Fig. 8, which were produced 378 from a series of tests in which a collimated  $^{60}\text{Co}$  source was placed at seven different locations along a 379 scintillator. One of the two coincident photons emitted 380 by  $^{60}\text{Co}$  reaches the scintillator and the other is detected 381 by an auxiliary detector serving as the trigger. The photons 382 incident on the scintillator have a spot size of less than 1 cm due to source collimation. These events all

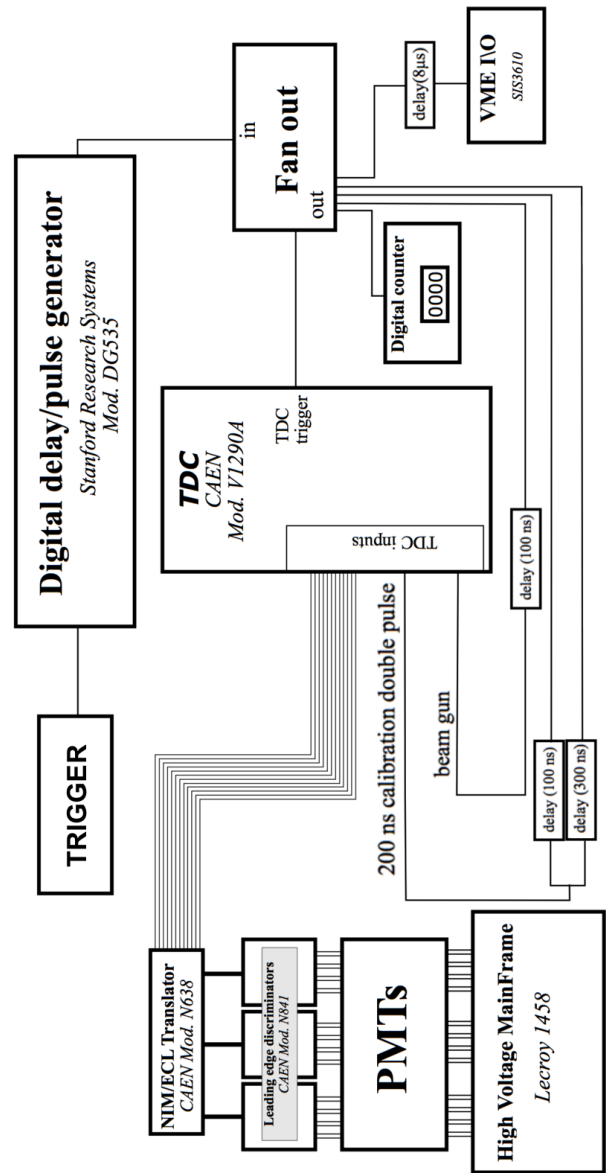
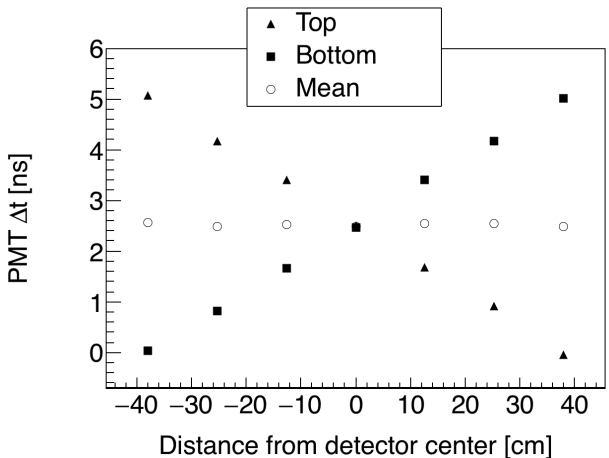


FIG. 7: Wiring diagram of the electronics setup.

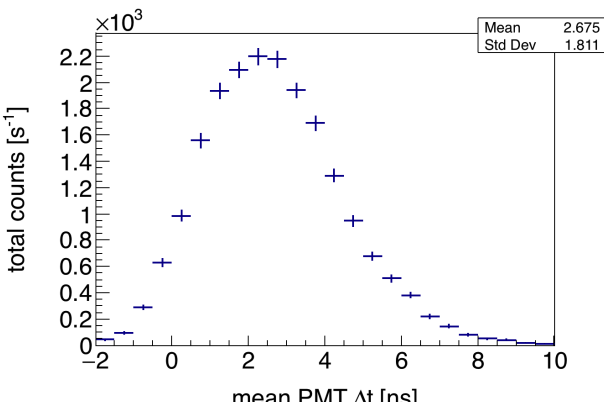
385 have equal transit time, regardless of the  $^{60}\text{Co}$  source's 386 position.

387 In Figure 8(a), it can be seen that the time required 388 for the scintillation light to propagate along the scintillator 389 has a large effect on the timing of each PMT alone,  
 390 however, the average of the times of both PMTs is a constant, 391 unaffected by the location at which the particle 392 undergoes scintillation. For this reason, taking the average 393 age of signals from two PMTs is advantageous because it 394 removes the roughly 5 ns timing error that would otherwise 395 exist due to the time required for scintillation light 396 to propagate along the scintillator. The requirement that 397 there be coincident events in both of a detector's PMTs 398 also aids in reducing noise.

399 During photofission measurements, ToF is calculated



(a)



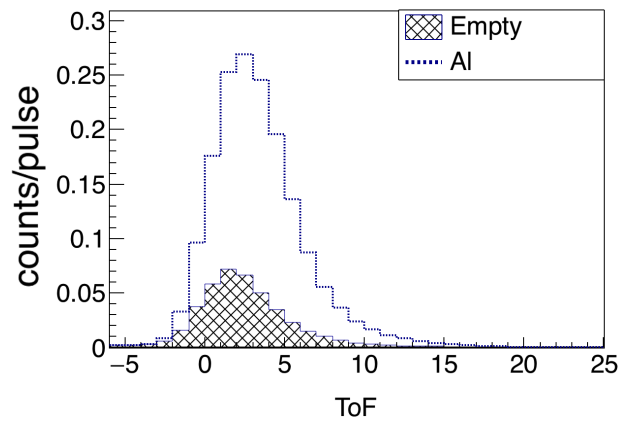
(b)

**FIG. 8:** A collimated  $^{60}\text{Co}$  source is used to produce photon events with constant ToF at seven locations along the detector.  $^{60}\text{Co}$  produces coincident photons, and one is detected by the scintillator and the other by a separate trigger detector.  $\Delta t$  is the timing of a PMT signal relative to a signal from the trigger detector. In (a), it can be seen that the average between signals from both PMTs does not depend on position. By using the PMT average, there is a reduction in error due to the time required for scintillation light to travel along the scintillator. The uncertainty in ToF measurements is equal to the standard deviation seen in (b), or about  $\pm 2$  ns, because all photons from the  $^{60}\text{Co}$  source have the same ToF.

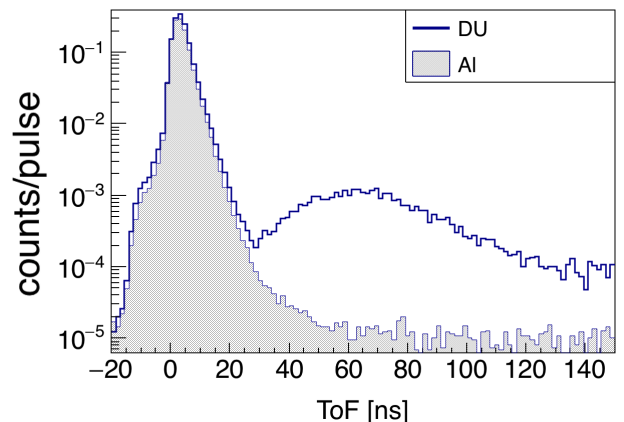
401 by the following expression:

$$\text{ToF} = t_{\text{mean}}^{\text{PMTs}} - t_{\text{beam}} + C, \quad (1)$$

402 where  $t_{\text{mean}}^{\text{PMTs}}$  is the mean of the times of signals from  
403 both PMTs of a scintillator,  $t_{\text{beam}}$  is the time of a sig-  
404 nal provided by the accelerator at the beginning of each  
405 pulse, and  $C$  is a constant timing offset. Any process that  
406 produces a timing delay that does not change from pulse  
407 to pulse contributes to  $C$ . For example, the time required  
408 for photons to travel from the bremsstrahlung radiator to  
409 the target, the propagation of signals through the cables



(a)



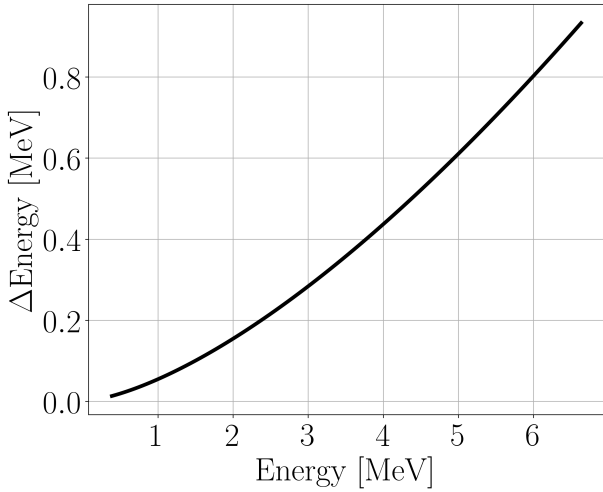
(b)

**FIG. 9:** (a) Comparison between the ToF spectrum of a non-neutron producing target made from Al, to the ToF spectrum produced when no target is used. The large increase in events around 4 ns is due to photons that scatter from the Al target. When no target is in place, sources of the peak seen here is used to find the timing offsets that make it so  $t = 0$  corresponds to the moment of fission. (b) Comparison between the Al and DU targets show a pronounced increase in events for DU between 35 and 130 ns due to the introduction of neutrons.

410 connecting the PMTs, delays in the electronics, *etc.*

411 The value of  $C$ , which may be different for each de-  
412 tector, is determined by comparing the timing spectra  
413 of the gamma flash produced by a non-neutron produc-  
414 ing aluminum target, to that produced when no target  
415 is used (see Fig. 9). The difference between these two  
416 spectra reveals a prominent peak in the ToF spectrum  
417 due to photons that scatter from the aluminum target.  
418 These photons must travel 125 cm to reach the center of  
419 any detector and 130 cm to reach the top, for which it  
420 takes light 4.2 ns and 4.3 ns to travel, respectively. The  
421 value of  $C$  used for each detector is equal to the value  
422 that places the time corresponding to the peak of the  
423 target-induced gamma flash at 4 ns.

424 The kinetic energy of a detected neutron is determined



(a)

**FIG. 10:** Uncertainty in neutron energy measurements as a function of measured neutron energy.

straightforwardly from its velocity, which is determined from its ToF under the assumption that the neutron traveled directly from the target to the detectors unimpeded. According to a series of MCNP simulations examining the scattering of fission neutrons within detector shielding and the fission target, neutrons predominantly travel to the detectors unimpeded. These simulations are discussed in sections IID and II A.

Figure 10 shows the measurement uncertainty in neutron energy due to error in the ToF determination.

## B. Particle Position Reconstruction

Each detector is not capable of measuring the position of a detected particle along the axes parallel to its width (15.24 cm) or depth (3.81 cm), which contributes  $\pm 3^\circ$  to the total angular uncertainty. The position of a detected particle along the 76.2 cm length of the scintillator is calculated using the timing difference of signals from both of a detector's PMTs. Assuming that scintillation light travels from an initial point, let it be  $x$  cm from the center of a scintillator, to both PMTs at a velocity that is constant with respect to the scintillator's length-wise axis, then the difference between the times at which the light will reach each PMT ( $\Delta t^{PMTs}$ ) is given by:

$$\begin{aligned} \Delta t^{PMTs} &= t^{PMT_1} - t^{PMT_2} \\ &= \frac{(L/2 + x)n_{\text{eff}}}{c} - \frac{(L/2 - x)n_{\text{eff}}}{c} \\ &= 2x \frac{n_{\text{eff}}}{c}. \end{aligned} \quad (2)$$

Solving for  $x$  gives

$$x = \frac{c}{2n_{\text{eff}}} \Delta t^{PMTs}, \quad (3)$$

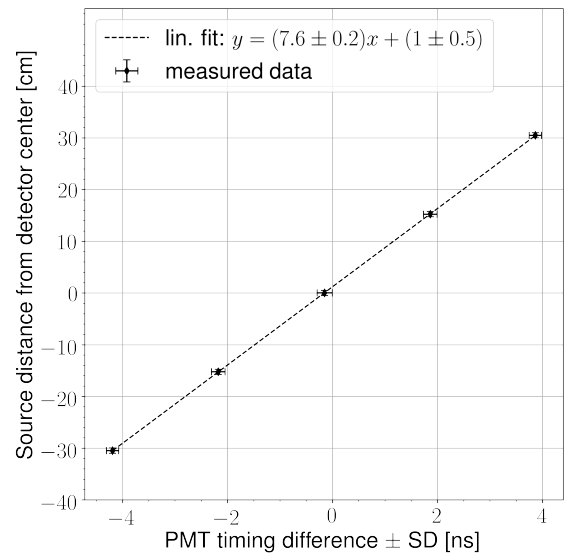


**FIG. 11:** A collimated  ${}^{60}\text{Co}$  source is used to produce photon events at five different positions along the scintillator. The mean PMT timing difference of events at each position varies linearly with respect to the distance of the  ${}^{60}\text{Co}$  source from the center of the detector. The result of a linear least squares fit to this data is used to calculate the position of detected particles along the length of each scintillator.

where  $t^{PMT_1}$  and  $t^{PMT_2}$  are the times of signals from each of a detector's PMTs relative to the accelerator gun pulse,  $L$  is the length of the scintillator,  $c$  is the speed of light,  $n_{\text{eff}}$  is the effective index of refraction of the scintillation material. A linear least squares fit between  $x$  and  $\Delta t^{PMTs}$  was performed on data gathered using coincident photons emitted by a collimated  ${}^{60}\text{Co}$  source, as described in the previous section. The resulting fit parameters, seen in Fig. 11, are used to find the position of detected particles.

Using the slope of the linear fit in Fig. 11, along with Eq. 3, an effective index of refraction of the scintillation material is calculated to be 2.0. This index of refraction is said to be “effective” because its measurement is sensitive only to the scintillation light’s average speed projected onto the axis parallel to the scintillator’s longest dimension, which is equal to the intrinsic speed of light in the material only if the light is traveling parallel to the scintillator’s length. While the detection of scintillation light by both PMTs favors light paths which are parallel or nearly-parallel to the scintillator’s length, there is some reflection of detected scintillation light from the boundaries of the scintillator. This effect contributes to the  $\pm 9$  cm measurement uncertainty in particle position reconstruction. As a result of these effects, the index of refraction measured here is  $\sim 25\%$  greater than the true value of the scintillation material.

478

### C. Measurements with $^{252}\text{Cf}$

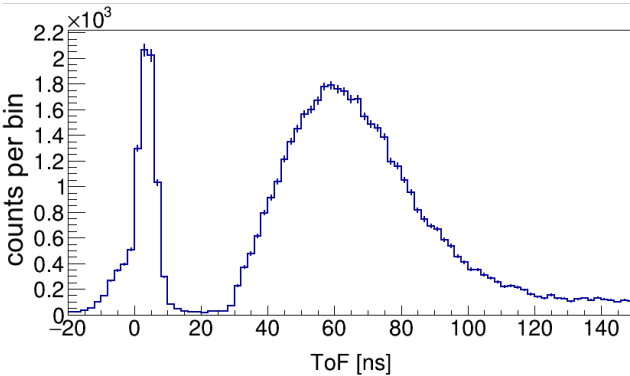


**FIG. 12:** Measured ToF spectrum from the SF of  $^{252}\text{Cf}$ . The sharp peak on the left is due to fission photons, followed by another peak due to fission neutrons.

A  $^{252}\text{Cf}$  source was placed at the center of the detection system shown in Fig. 2 in order to measure the n-n opening angle distribution. Several such past measurements have been performed (see Refs. [7–10]), and serve as a means to validate the methods used throughout this study.

The  $^{252}\text{Cf}$  source produces a cleaner ToF spectrum than photofission due to the lack of beam related backgrounds (see Fig. 12), and therefore these measurements have a better signal to noise ratio. Also, there is no concern over the detection of accidental neutron coincidences because the fission rate of the  $^{252}\text{Cf}$  source was about 3,500 fissions/s, making it highly unlikely that multiple fissions will occur during the electronic acceptance time window of 150 ns. The beginning of the 150 ns neutron acceptance time window was triggered by a 2-fold coincidence, within a 4 ns window, between two separate  $10 \times 10 \times 5 \text{ cm}^3$  plastic scintillators, one placed above and the other below the source at a distance of 30 cm. Aside from this difference in the time window triggering mechanism, identical methods were used for both photofission and SF measurements.

501

## IV. ANALYSIS

The efficiency and acceptance of the neutron detection system varies greatly over its opening angle range of  $20^\circ$  to  $180^\circ$ , as illustrated in Fig. 13. This is both due to the neutron detection system's non-spherical symmetry and to varying efficiency as a function of particle position on the detector. In order to give a result that is sensitive to angular correlations, but is highly insensitive to detector efficiencies and experimental drifts in PMT voltage, accelerator current, etc., the angular correlation is determined by dividing a correlated neutron distribution by

an uncorrelated neutron distribution. That is,

$$\text{angular correlation} = \frac{nn_{\text{corr}}(\theta)}{nn_{\text{uncorr}}(\theta)}, \quad (4)$$

where  $nn_{\text{corr}}(\theta)$  is the n-n yield after the subtraction of accidental n-n coincidences, and  $nn_{\text{uncorr}}(\theta)$  is a contrived distribution of uncorrelated n-n pairs, which is produced by pairing neutron events that occurred during different pulses. The subtraction of accidental n-n coincidences to produce  $nn_{\text{corr}}(\theta)$  amounts to a 10% correction, the procedure of which is covered in section IV B. The construction of  $nn_{\text{uncorr}}(\theta)$  is described in detail in section IV A.

**522 A. Cancelation of Detector Efficiencies, Drifts, and  
523 Geometric Phase Space**

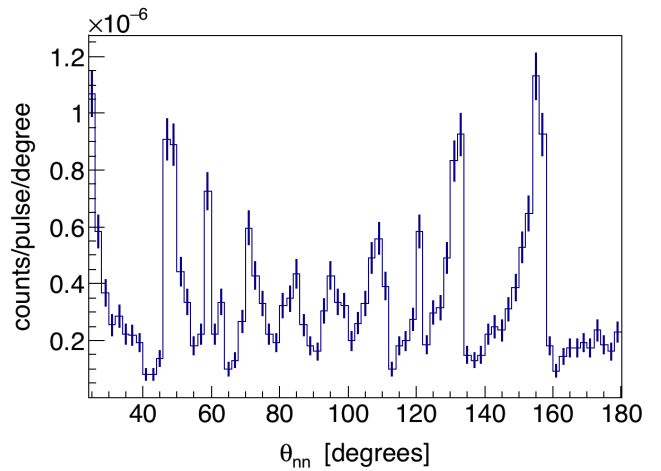


**FIG. 13:** Raw n-n opening angle yield from the photofission of  $^{238}\text{U}$ . This distribution is highly influenced by the detection system's geometric acceptance and efficiency.

The construction of  $nn_{\text{uncorr}}(\theta)$  is achieved by pairing detected neutrons that were produced during different accelerator pulses. The same set of pulses used for  $nn_{\text{corr}}(\theta)$  is used here, so each of these pulses individually consist of the detection of two coincident neutrons. When constructing  $nn_{\text{uncorr}}(\theta)$ , it is desirable that the neutrons comprising each uncorrelated n-n pair originated from different pulses that occurred as closely together in time as possible. A smaller time difference between pulses that are paired for this purpose increases the chance that both neutrons were detected under the same experimental conditions amid any drifting of accelerator current, PMT voltages, and varying rates of noise. However, some time difference between the pulses must be allowed so as not to cause insufficient counting statistics. Accordingly, uncorrelated n-n pairs used to construct  $nn_{\text{uncorr}}(\theta)$  are formed by neutrons that were detected within 30 minutes or less of each other.

Uncorrelated n-n pairs will have a slightly different joint energy distribution than correlated n-n pairs, which could affect the extent to which the effects of detector efficiency cancel in Eq. 4. This issue is addressed in section V A, where it is shown that these differences have little potential to significantly affect the final result.

Figure 14(a) shows the measured yield distribution of correlated neutrons,  $nn_{\text{corr}}(\theta)$ , from the photofission of  $^{238}\text{U}$ . The structure seen here is reflective of the underlying n-n angular correlations as well as the geometric acceptance and efficiencies of the neutron detectors. Figure 14(b) reveals how a clear picture of n-n angular correlations emerges when taking the ratio between  $nn_{\text{corr}}(\theta)$  and  $nn_{\text{uncorr}}(\theta)$ . Applying the same technique to a measurement of coincident neutrons from the photodisintegration of  $\text{D}_2\text{O}$  produces a flat line as expected (see Fig. 15), as in this case all neutron coincidences are accidental.

## 560 B. Subtraction of Accidental Coincidences

The observation of two uncorrelated signals in the neutron ToF range, whether caused by neutrons, photons, or noise, is referred to as an *accidental coincidence*. Accidental coincidences due to noise and photons, which are estimated using a non-neutron producing aluminum target (see Fig. 16), amount to about 3% of all coincidences. Accidental coincidences due to neutrons are minimized by adjusting the accelerator's current so that there are, on average, less than 1.0 fissions per accelerator pulse. Nevertheless, statistical fluctuations in the number of fissions per pulse result in the production of accidental coincident neutrons that originated from different, and therefore, uncorrelated fissions. There are also accidental neutron coincidences caused by the occurrence of multiple  $(\gamma, n)$  reactions in a single pulse. The energy integrated  $(\gamma, n)$  cross-section of  $^{238}\text{U}$ , weighted by the bremsstrahlung energy distribution, is about a factor of 5.5 times greater than it is for photofission (see Fig. 17). As a result, the raw n-n coincident yield will contain a significant number of n-n coincidences from multiple  $(\gamma, n)$  reactions in relation to n-n coincidences from fission. The presence of accidental n-n coincidences has the effect of washing out the signal from correlated neutrons.

The raw measurement of n-n yield consists of a mix of correlated and accidental neutron coincidences, that is

$$nn_{\text{raw}}(\theta_{nn}) = nn_{\text{corr}}(\theta_{nn}) + nn_{\text{acc}}(\theta_{nn}), \quad (5)$$

where  $nn_{\text{raw}}(\theta_{nn})$  and  $nn_{\text{acc}}(\theta_{nn})$  are the per-pulse n-n yields as a function of opening angle,  $\theta_{nn}$ , for all detected n-n pairs, and detected accidental n-n pairs, respectively. As already defined,  $nn_{\text{corr}}(\theta_{nn})$  is the per-pulse yield of detected correlated n-n pairs.

Because the n-n coincidences comprising  $nn_{\text{acc}}(\theta_{nn})$  consist of two independent detected neutrons, they are governed by the exact same physics and are subject to

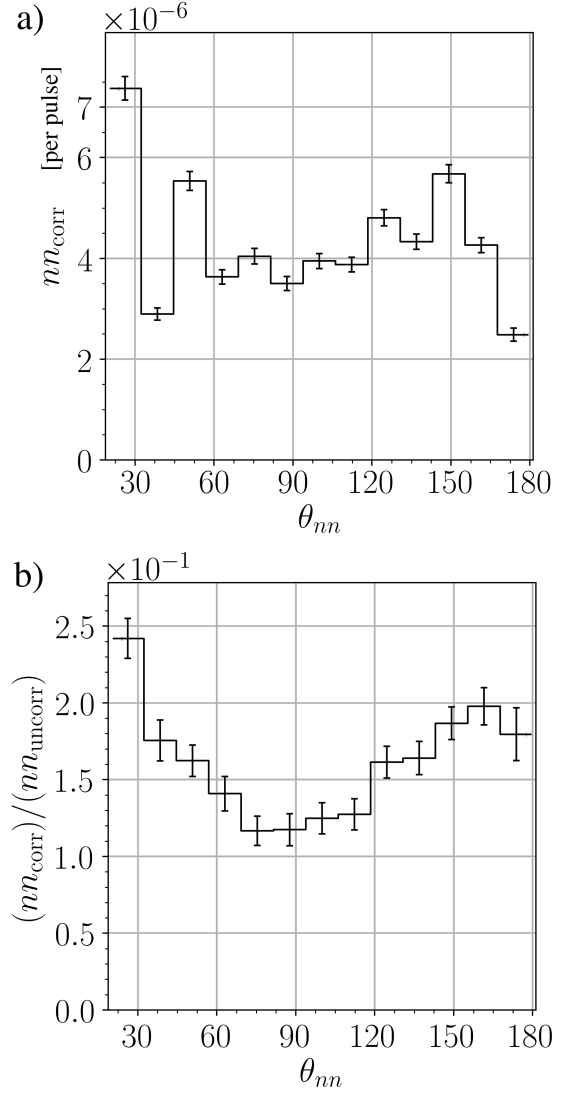


**FIG. 14:** n-n opening angle distribution from the photofission of  $^{238}\text{U}$  before the normalization procedure seen in Eq. 4 (a), and after normalization (b). All measured neutrons have an energy greater than 0.4 MeV.

the exact same experimental conditions as n-n coincidences formed by pairing of single neutrons that were detected during different pulses. Therefore, the opening angle distribution formed by pairing neutrons that were detected during different pulses, denoted  $nn_{dp}(\theta_{nn})$ , is proportional to  $nn_{\text{acc}}(\theta_{nn})$ .  $nn_{dp}(\theta_{nn})$  is constructed from the set of all possible pulse-pairs formed by pulses that occurred within 0.2 seconds of each other. The restriction in time difference is applied in order to increase the chance that pulse pairs together occurred under similar experimental conditions. There are no other restrictions on which pulses can be used in this case. Many

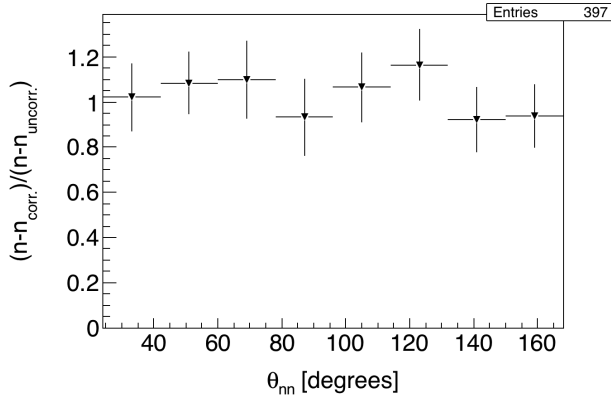


**FIG. 15:** A measurement of the angular correlation of uncorrelated neutrons emitted by the photodisintegration of  $\text{D}_2\text{O}$  gives the expected uniform distribution.

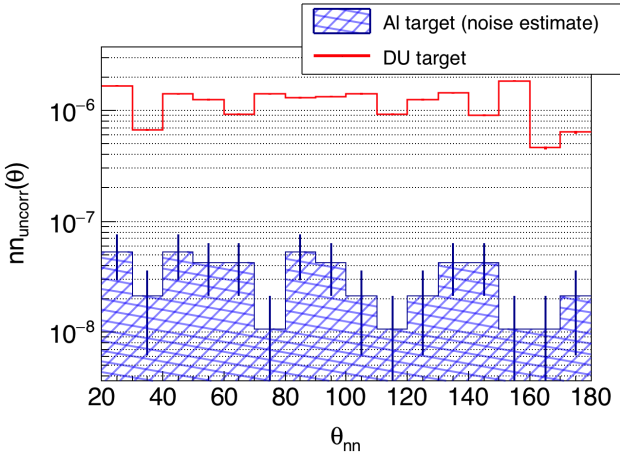


**FIG. 16:** An Al target was designed to have the same thickness, in radiation lengths, as the  $^{238}\text{U}$  target, thus serving as an equivalent non-neutron producing target well-suited for noise estimates. The rate of the detection of coincident events in the neutron ToF range while using the Al target was 3% that of the  $^{238}\text{U}$  target. Thus, 3% of coincident events used in the determination of n-n angular correlations in  $^{238}\text{U}$  can be attributed to noise.

608 pulse-pairs used for the construction of  $nn_{dp}(\theta_{nn})$  will  
609 contain no detected neutrons.

610 While  $nn_{dp}(\theta_{nn})$  and  $nn_{acc}(\theta_{nn})$  are proportional,  
611  $nn_{acc}(\theta_{nn})$  is not equal to  $nn_{dp}(\theta_{nn})$ , because there are,  
612 on average, more detected neutrons per pulse-pair than  
613 per pulse. As the following analysis shows,  $nn_{acc}(\theta_{nn}) =$   
614  $\frac{1}{2}nn_{dp}(\theta_{nn})$ , under the condition that  $nn_{acc}(\theta_{nn})$  is nor-  
615 malized to the number of pulses and  $nn_{dp}(\theta_{nn})$  to the  
616 number of pulse-pairs considered. When looking at single  
617 pulses, the probability of there being a detected uncorre-  
618 lated n-n pair is denoted by  $P_{sp}^{\text{n-n}}$ , and when looking at  
619 pulse-pairs, by  $P_{dp}^{\text{n-n}}$ . Thus,  $P_{sp}^{\text{n-n}}$  and  $P_{dp}^{\text{n-n}}$  determine the  
620 relative rates of  $nn_{acc}(\theta_{nn})$  and  $nn_{dp}(\theta_{nn})$ , respectively.

621 The statistics of the detected uncorrelated neu-  
622 trons per pulse is assumed to follow a Poisson distribu-

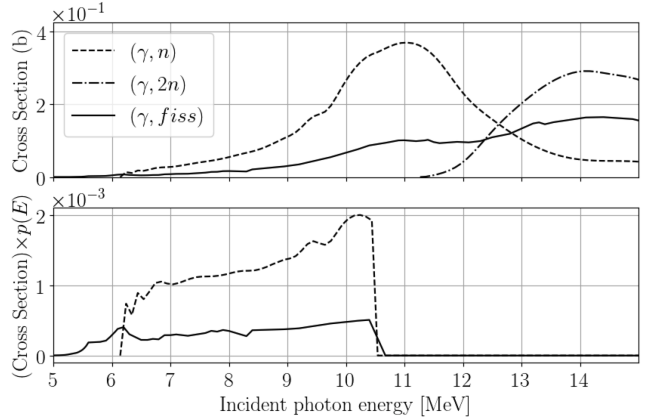


**FIG. 17:** (top) ENDF cross-sections of  $(\gamma, \text{fiss})$ , direct  $(\gamma, \text{n})$ , and direct  $(\gamma, 2\text{n})$ . (bottom) Cross-sections weighted by the simulated relative rate of bremsstrahlung photons that reach the target as a function of photon energy. The integrated cross-sections of  $(\gamma, \text{n})$  is 5.5 times greater than for  $(\gamma, \text{fiss})$ . Assuming a  $\bar{\nu}$  of 2 neutrons/fission, the bremsstrahlung beam produces about 2.7 times more neutrons via  $(\gamma, \text{n})$  than  $(\gamma, \text{fiss})$  within the target.

623 tion, which describes the occurrence of independent ran-  
624 dom events. Accordingly, the probability of the detection  
625 of  $k$  uncorrelated neutrons in a given pulse is

$$p(k) = \frac{e^{-\lambda} \lambda^k}{k!}, \quad (6)$$

626 where  $\lambda$  represents the mean number of uncorrelated de-  
627 tected neutrons per pulse. In principle,  $\lambda$  equals the total  
628 number of detected uncorrelated neutrons divided by the  
629 total number of pulses. Determination of  $\lambda$  cannot be  
630 done in practice, because one would need to know which  
631 pairs of detected neutrons are correlated. However, the  
632 largest possible value for  $\lambda$  is the total number of de-  
633 tected neutrons divided by the total number of pulses, as  
634 this quantity counts all detected neutrons, whether they  
635 are correlated or uncorrelated. For this work, that places  
636 an upper bound on  $\lambda$  of  $5.5 \times 10^{-3}$  detected uncorrelated  
637 neutrons per pulse, which is small enough to truncate all  
638 terms beyond the leading term in the following analysis.

639 Because  $P_{sp}^{\text{n-n}}$  represents the probability of the detec-  
640 tion of two uncorrelated neutrons in a single pulse,  $P_{sp}^{\text{n-n}}$   
641 is equal to  $p(2)$ , as per Eq. 6. Thus,

$$\begin{aligned} P_{sp}^{\text{n-n}} &= \frac{e^{-\lambda} \lambda^2}{2!} \\ &\approx \frac{\lambda^2}{2} + \mathcal{O}(\lambda^3). \end{aligned} \quad (7)$$

642 When considering the case of  $P_{dp}^{\text{n-n}}$ , recall that, in  
643 this case, uncorrelated n-n pairs are formed by exam-  
644 ining pulse-pairs. Here, an uncorrelated n-n pair occurs  
645 when there is a detected neutron in both pulses. Because  
646 all terms beyond the leading term are being truncated,  
647 pulse-pairs in which one or both of the pulses comprise

two or more detected neutrons do not need to be considered. Thus,  $P_{dp}^{n-n}$  is equal to the probability of there being exactly one detected neutron in each pulse, which is the square of the probability of there being exactly one detected neutron in a single pulse, namely,  $p(1)^2$ . Thus, again using Eq. 6,

$$\begin{aligned} P_{dp}^{n-n} &= (e^{-\lambda} \lambda)^2 \\ &\approx \lambda^2 + \mathcal{O}(\lambda^3). \end{aligned} \quad (8)$$

Because  $P_{dp}^{n-n}$  and  $P_{sp}^{n-n}$  determine the relative rates of  $nn_{dp}(\theta_{nn})$  and  $nn_{acc}(\theta_{nn})$ , respectively, and because the two distributions have the same shape, from Eq.'s (8) and (7), it follows that

$$nn_{acc}(\theta_{nn}) = \frac{1}{2} nn_{dp}(\theta_{nn}). \quad (9)$$

Finally, from Eq.'s 9 and 5, the distribution of solely correlated n-n pairs can be recovered from the raw measurement as follows

$$nn_{corr}(\theta_{nn}) = nn_{raw}(\theta_{nn}) - \frac{1}{2} nn_{dp}(\theta_{nn}). \quad (10)$$

## 561 V. POTENTIAL SOURCES OF ERROR

### 562 A. Correlated versus uncorrelated n-n energy 563 distribution

In order to effectively minimize the dependence of the result on detector geometry/efficiency, the numerator and denominator of Eq. 4 must comprise neutron pairs with a similar energy distribution. Note that accidental coincident neutrons from  $(\gamma, n)$  are completely removed from  $nn_{corr}(\theta)$ , the numerator in Eq. 4, by the subtraction of accidental coincidences, but are not removed from the denominator,  $nn_{uncorr}(\theta)$ . This is the reason for using only pulse-pairs that have two events in each pulse when determining the uncorrelated neutron distribution. Doing so increases the selection of neutrons from fission as opposed to  $(\gamma, n)$ .

When examining differences between the neutron energy distributions in  $nn_{corr}(\theta)$  and  $nn_{uncorr}(\theta)$ , it is important to consider how the energies of both neutrons forming n-n pairs vary together, or, in other words, their joint energy distribution. Figure 18 shows the ratio between the rates for correlated and uncorrelated n-n pairs of various binned energies. The effect that these discrepancies in energy distribution have on the final result can be examined by applying a weighting factor to each event in  $nn_{uncorr}(\theta)$  such that a recalculation of the result in Fig. 18 produces a flat curve. A comparison of the angular correlation with and without the application of these weighting factors to uncorrelated n-n events is seen in Fig. 19. The resulting weighted distribution is identical within experimental uncertainties to the unweighted distribution, suggesting that differences in the energy distri-

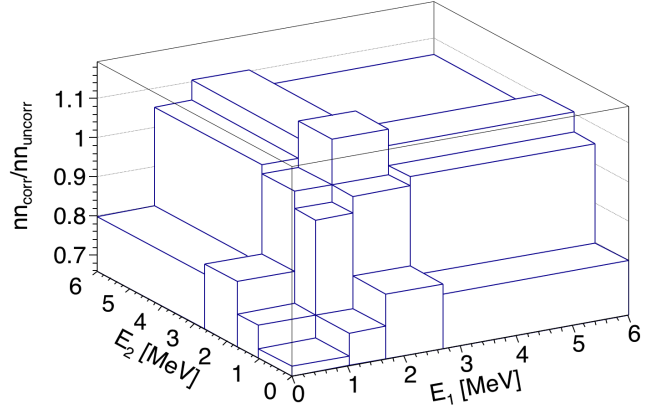


**FIG. 18:** The z-axis represents the ratio between the correlated and uncorrelated rates of binned n-n energies. The energy bins are chosen such that each contains an equal number of events, or 1/16th of the total events.

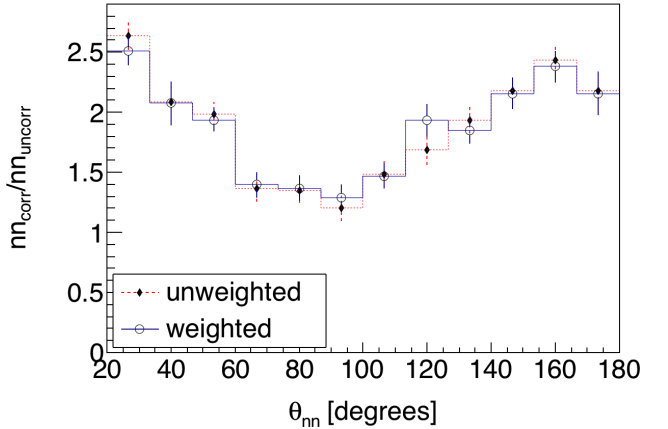


**FIG. 19:** Each uncorrelated n-n event can be weighted such that the weighted histograms of the joint n-n energy distributions of correlated and uncorrelated n-n pairs are equal. Comparison of the calculated angular correlation results, with and without such weighting factors applied to all uncorrelated n-n events, illustrates that any effects due to the discrepancies in the joint energy distributions of correlated and uncorrelated n-n pairs are negligible.

butions of  $nn_{corr}(\theta)$  and  $nn_{uncorr}(\theta)$  do not significantly affect the present measurement.

### 696 B. Detector Cross-talk

*Cross-talk* occurs when, after a particle is detected once, the same particle, by any means, causes a detection to be registered in a different detector. For example, upon detection, a particle may undergo elastic scattering and then travel into another detector where it is detected again, or, it may produce secondary particles that are detected. The two coincident detections of a cross-talk event are causally correlated, and thus they have the potential to contaminate the signal from correlated fission

neutrons. If both detections occur during the ToF range typical for fission neutrons, then the cross-talk event cannot be distinguished from the detection of two correlated neutrons.

Recent works that measured the n-n angular correlations in the spontaneous fission of  $^{252}\text{Cf}$  and  $^{240}\text{Pu}$  [10, 12] addressed this effect by using an MCNP-PoLiMi simulation to estimate and then subtract cross-talk from their measurements. In this work, the issue of cross-talk is approached differently by employing the use of detector shielding aimed at reducing cross-talk to a negligible rate. By using shielding to reduce cross-talk, this measurement is less dependent on the details of the models used by MCNP-PoLiMi to simulate neutron transport and detection. MCNP-PoLiMi simulations are used in this work only to verify that the effect of cross-talk is negligible.

The scintillators used here are much larger than those used in similar works, such as in Refs. [10, 12], allowing them to be placed much farther from the fission source without causing a detrimental loss in coincidence rates. An increase in the distance between the detectors and the fission source makes this measurement less subject to angular uncertainty, which depends directly on the uncertainty in the position of a detected particle due to, for example, the scattering of neutrons from detector shielding. For this reason, larger amounts of shielding can be used without concern of introducing large errors.

Furthermore, the geometry of the neutron detection system makes it kinematically impossible for a neutron to undergo a single scattering event with a proton in one detector, which is the basis for scintillation, and then travel directly into another detector with enough kinetic energy to be detected a second time. For this reason, upon being detected, a neutron must scatter from one or more intermediate nuclei, such as lead or carbon, in order for it to reach another detector with enough energy to be detected again. This fact follows from the conservation of energy and momentum. In order to support the claim that the design of the neutron detection system reduced cross-talk to negligible rates, a detailed MCNP-PoLiMi [16] simulation was performed in which a built-in  $^{252}\text{Cf}$  source is positioned at the center of a model of the neutron detection system.

### 1. Simulation of Detector Cross-talk

The cross-talk simulation included all scintillators, shielding, detector supporting structures, and the concrete walls surrounding the experimental cell. MCNP-PoLiMi's built-in  $^{252}\text{Cf}$  spontaneous fission source was used, which emits neutrons with the correct correlations and multiplicities according to previous measurements. Detector response was modeled using a program included with the MCNP-PoLiMi distribution called MP-Post [17]. The model is based on the MeV electron equivalent (MeVee) light output produced by particles as they undergo collisions with carbon and hydrogen within or

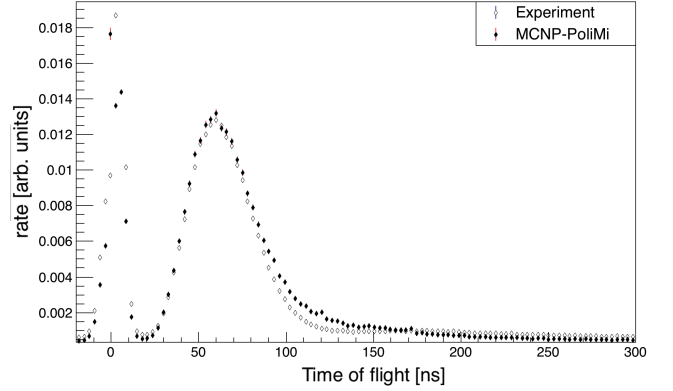


**FIG. 20:** Measured *versus* simulated ToF spectrum from the SF of  $^{252}\text{Cf}$ . The simulation used the detector response model outlined in ref [17]. The simulated and measured curves are normalized in order to facilitate comparison.

ganic plastic scintillators. A minimum deposited energy of 0.4 MeV (equivalent to 0.05 MeVee for neutrons) was assumed for detectable particles, which was chosen because the neutron detection system exhibited a sharp decline in detection efficiency for neutrons below 0.4 MeV.

For neutron collisions with hydrogen, the light output in MeVee, denoted  $L$ , is calculated by the following empirically derived formula [17]

$$L = 0.0364\Delta E_n^2 + 0.125\Delta E_n ,$$

where  $\Delta E_n$  is equal to the loss in the kinetic energy of the neutron due to the collision. Neutron interactions with carbon are assumed to generate a small light output of

$$L = 0.02\Delta E_n .$$

As seen in Fig. 20, this model of the detection process produces a ToF spectrum for the SF of  $^{252}\text{Cf}$  that shows good agreement with the measurement for neutrons with a ToF less than 100 ns and fair agreement for neutrons with a ToF greater than 100 ns.

Figure 21 shows the distribution of cross-talk events and true n-n coincidences as a function of reconstructed opening angle. It is worth noting that, according to this simulation, the effect of cross-talk is not only small, but is also distributed over a wide range of n-n opening angles rather than being concentrated around 0 degrees as one might expect. Angles greater than 125 degrees are not shown in Fig. 21 because cross-talk events at large angles can be readily identified in analysis due to the large amount of time required for a neutron to travel these distances. The simulation was initially performed with 5 cm of lead shielding placed behind the scintillators, and the number of cross-talk events accounted for 11% of the total coincident neutron events. This value fell to 3% when polyethylene was used instead of lead, motivating the placement of 10 cm of polyethylene behind the detectors instead of lead.

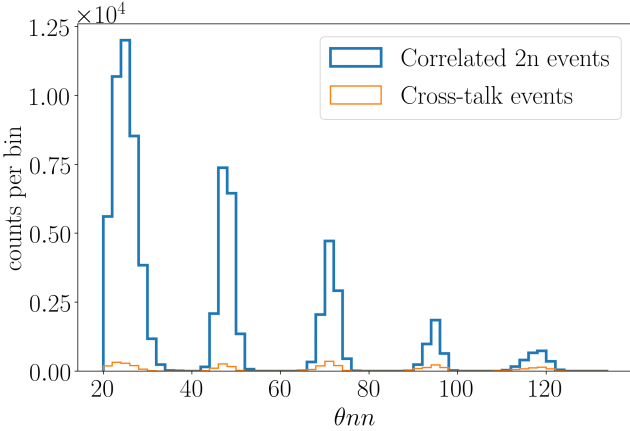


**FIG. 21:** MCNP-PoLiMi simulation of the number of cross-talk events *versus* correlated n-n events as a function of reconstructed opening angle. Cross-talk accounted for 3% of total events. Simulated cross-talk events do not occur primarily at small angles, but are instead spread out over a wide range of angles. Any cross-talk occurring at angles larger than  $125^\circ$  will be removed from the experimental data by the cuts applied to neutron ToF.

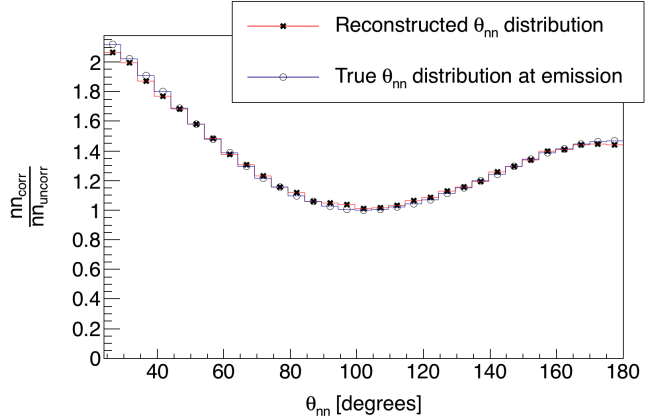


**FIG. 22:** MCNP-PoLiMi simulation of correlated  $^{252}\text{Cf}$  neutrons sampled uniformly throughout a  $0.05 \times 2 \times 4 \text{ cm}^3$  U-238 target. The slight difference between the curves is due solely to the elastic scattering of neutrons within the target, since detector physics was not simulated. In the reconstructed  $\theta_{nn}$  distribution ( $\star$ ), only neutrons which enter a physical volume at which a detector was located during the experiment are counted. The true  $\theta_{nn}$  distribution at the moment of emission is also plotted ( $\circ$ ).

### 796 C. Neutron Scattering within the Target

797 A potential source of error in opening angle measurements is the scattering of emitted neutrons as they tra-  
798 vers the fission target. This is cause for concern because  
799 when neutrons scatter from heavy nuclides such as  $^{238}\text{U}$ ,  
800 they are likely to be deflected at large angles resulting in  
801 n-n opening angles that do not reflect the true underlying  
802 fission kinematics. The effect that this has on this work  
803 is assessed by MCNP simulations. In summary, for 6% of  
804 n-n pairs, at least one neutron out of the two scatters be-  
805 fore exiting the target, according to the simulation. This  
806 effect does not have a large influence on the measured  
807  $\theta_{nn}$  distribution according to the simulation data shown  
808 in Fig. 22.

809 The rate of elastic scattering is affected by the size  
810 and shape of the target. A thin strip is the ideal target  
811 shape regarding the rate of neutron elastic scattering per  
812 unit of total target volume. See Fig. 23 for the simulated  
813 elastic scattering rates for both thin strip and cylindrical  
814 shaped targets. The simulation indicates that the rate of  
815 elastic scattering in cylindrical targets is about a factor  
816 of two times greater than in thin strip targets with the  
817 same volume.

818 The target's dimensions are small enough that the  
819 rate of photon absorption, and thus photo-neutron pro-  
820 duction, is virtually uniform throughout the entire tar-  
821 get volume. An MCNP-PoLiMi simulation was used  
822 to generate  $^{252}\text{Cf}$  spontaneous fission events uniformly  
823 throughout the target. The SF of  $^{252}\text{Cf}$  is used instead  
824 of the photofission of  $^{238}\text{U}$  because of the current lack  
825 of photofission models, however, the underlying fission  
826 kinematics are, broadly speaking, the same for the SF of  
827  $^{252}\text{Cf}$  and the photofission of  $^{238}\text{U}$ . Thus, the two pro-

831 cesses have similar n-n correlations.

832 Section VI B discusses the observation of an unex-  
833 pected drop in correlation around  $180^\circ$  n-n opening an-  
834 gle for the photofission of  $^{238}\text{U}$ , as seen in Figs. 24 and  
835 25. This motivated a second simulation regarding elastic  
836 scattering which examined whether this decrease in the  
837 correlation around  $180^\circ$  opening angles reflects the un-  
838 derlying physics of the fission process. In particular, note  
839 that throughout these measurements, the target was con-  
840 tinuously rotated once per 8 seconds. This means that for  
841 the determination of the uncorrelated opening angle dis-  
842 tribution, the trajectories of the two neutrons were taken  
843 from two different pulses in which the target was at a dif-  
844 ferent orientation for each of them. Additionally, each of  
845 the neutrons likely originated from different regions of the  
846 target volume. On the other hand, for the same-pulse,  
847 correlated neutron measurement, the target was in the  
848 same orientation and the two neutrons were generated  
849 at the same position in the target. For these reasons,  
850 the rates of neutron scattering within the target are not  
851 necessarily equal for the same-pulse and different-pulse  
852 cases. As such, we investigated whether these differences  
853 could cause this apparent decrease in the opening angle  
854 distribution near  $180^\circ$ .

855 Using the correlated  $^{252}\text{Cf}$  SF source built-in to  
856 MCNP-PoLiMi, the opening angle distribution of neu-  
857 trons at the moment of emission, labeled *true* in Fig. 22,  
858 were compared to that of the neutrons after they have es-  
859 caped the target, labeled *reconstructed* in Fig. 22. The lo-  
860 cation of fission events were sampled uniformly through-  
861 out the target's volume. The analysis employs the same  
862 technique outlined in section IV A, in which a correlated  
863 neutron distribution is divided by an uncorrelated neu-

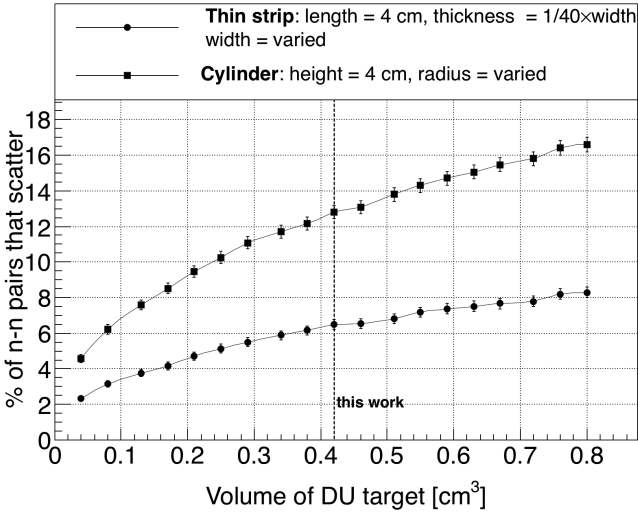


**FIG. 23:** Result of an MCNP simulation in which n-n pairs, with energies sampled from a typical watt fission spectrum, were generated uniformly throughout the volume of DU targets. The y-axis is the rate of opening angle contamination due to the scattering of, within the DU target in which they were produced, either one or both of a pair of neutrons. The lack of symmetry of a thin strip target can be removed by slowly rotating the target around the vertical axis during data acquisition, making it the optimal target geometry for the minimization of the rate of neutron scattering. The target used in this work had a length of 4 cm, a width of 2 cm, and a thickness of 0.05 cm.

tron distribution. The correlated neutron distribution is formed by pairing neutrons emitted during the same fission, and the uncorrelated distribution by the pairing of neutrons emitted during different fissions. In order to account for the effect of a rotating target on the trajectories of neutrons from different pulses, the coordinate system was rotated about the vertical axis accordingly for different fission events. The result from this simulation suggests that the rotating  $0.05 \times 2 \times 4 \text{ cm}^3$  U-238 target does not, due to neutron scattering, result in a measurable departure from the true n-n opening angle distribution.

876

## VI. RESULTS

877

### A. Comparisons with FREYA

The n-n opening angle correlation is calculated using the methods outlined in Sec. IV, in which a correlated neutron yield is divided by an uncorrelated yield. The results are compared with output from FREYA [18] (Fission Reaction Event Yield Algorithm), which was developed by the collaborative efforts of researchers from Lawrence Berkeley National Laboratory, Lawrence Livermore National Laboratory, Los Alamos National Laboratory, and University of Michigan Nuclear Engineering, and has been included in MCNP beginning with version

888 6.2.

The most recent release of FREYA (version 2.0.3) does not contain photofission directly, but instead uses neutron-induced fission as an *ad hoc* photofission model [19]. Representing photofission in this manner is a crude approximation, unsupported by experimental verification. Nonetheless, due to the current lack of accepted photofission models, the approximate approach, included in FREYA version 2.0.3, is compared with the results of the present work.

For a given nucleus with Z protons and A total nucleons, the code selects the neutron-induced fission model for a Z(A-1) nucleus, and chooses an incident neutron energy such that the compound ZA nucleus will have, relative to ZA's ground state, an excitation energy that is equal to the energy of the would-be incident photon.

When using FREYA to model photofission in this work, all model parameters, such as level density and partition parameters, were set to their default values for neutron-induced fission. FREYA was configured to use the fission fragment mass distribution,  $Y(A)$ , and the average total kinetic energy,  $\langle TKE \rangle(A)$ , from the  $^{238}\text{U}$  photofission measurements described in Ref. [20].

The measured  $\theta_{nn}$  distribution from the photofission of  $^{238}\text{U}$  and the SF of  $^{252}\text{Cf}$  are presented with the following two different types of cuts applied to the energies of neutrons in coincidence: in Figs. 24 ( $^{238}\text{U}$ ) and 26 ( $^{252}\text{Cf}$ ), a minimum energy threshold is applied to both neutrons, and in Figs. 25 ( $^{238}\text{U}$ ) and 27 ( $^{252}\text{Cf}$ ), the energy of both neutrons are required to fall within a specified range

In each of Figs. 24 through 27, the data are reported using two representations: the classic histogram and the kernel density estimate (KDE). When using a histogram to estimate a continuous distribution from the relatively small number of data points obtained in this work, one faces the following dilemma: small bin-widths lead to large uncertainties that are dependent on the chosen bin-width, while large bin-widths obscure potentially useful information. This problem is mitigated by the use of a KDE. A KDE is a method for estimating a continuous probability distribution from a finite set of sampled data points. The kernel was chosen to be the measurement errors in opening angle as determined by a study using coincident photons from a  $^{60}\text{Co}$  source, which was placed at different locations along a detector. The measurement errors in  $\theta_{nn}$  are well-described by a gaussian with a standard deviation of  $6^\circ$ . Mathematical details of the KDE method used in this work are outlined in Ref. [21]. The error bands seen in Figs. 24 through 27 correspond to 68% confidence intervals.

Plotted with each measurement is the result of a FREYA simulation. For the measurement of  $^{238}\text{U}$  photofission, there were a total of 2,952 n-n coincident events after the subtraction of accidentals, and for the SF of  $^{252}\text{Cf}$ , there were 21,882.

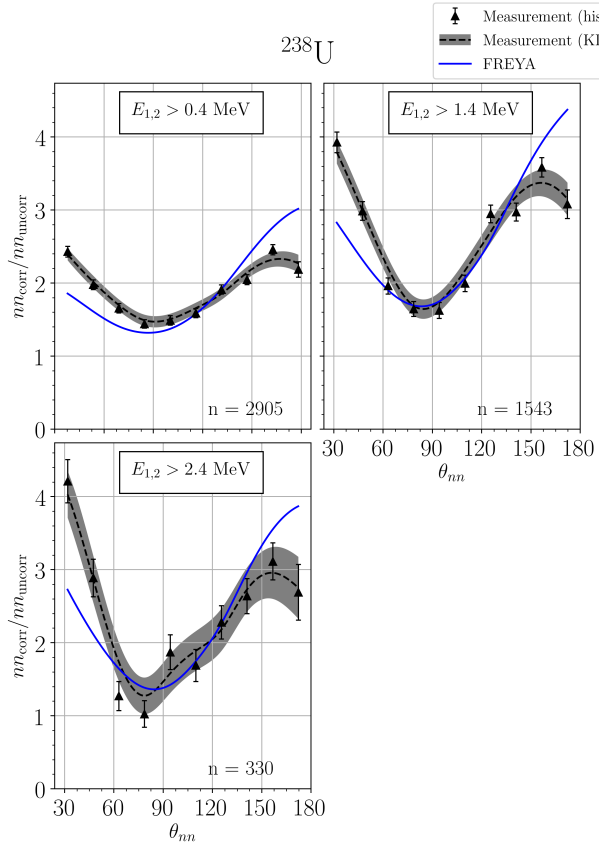


**FIG. 24:**  $\theta_{nn}$  distribution with minimum neutron energy cuts applied. The number of events contributing to each plot,  $n$ , is shown. Note that the bottom plots of this figure and Fig. 25 are identical.

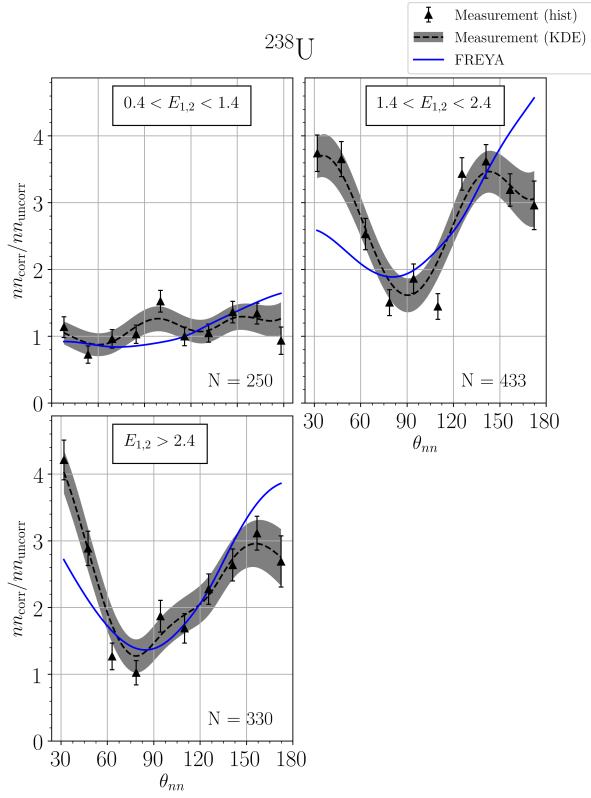


**FIG. 25:**  $\theta_{nn}$  distribution with cuts requiring that the energy of both coincident neutrons be within the specified range. The number of events contributing to each plot,  $n$ , is shown. Note that the bottom plots of this figure and Fig. 24 are identical.

## 943 B. Anomalous emission at large opening angles

944 While the results reported in the previous section are  
945 consistent with the effect of the kinematic focusing of the  
946 neutrons due to the recoil of the fission fragments, the  
947 data for U-238 show a statistically significant decrease  
948 in the n-n opening angle correlation in the region from  
949 about  $165^\circ$  to  $180^\circ$ , which can be seen in Figs. 14 and  
950 30, as well as in Figs. 24 and 25. The effect is particularly  
951 strong for the neutron energy cuts being applied in the  
952 upper right plots of both Figs. 24 and 25. A comparison  
953 of the observed decrease after  $160^\circ$  degrees with the null  
954 hypothesis that the true distribution remains constant  
955 after  $160^\circ$  degrees yields a p-value of 0.01. This indicates  
956 a 1% probability that the data are incompatible with a  
957 decrease in the correlation for large opening angles. This  
958 is a feature which does not seem to universally appear  
959 in either neutron-induced or spontaneous fission. A sim-  
960 ilar but less pronounced effect appears in the results re-  
961 ported in Ref. [11] for the thermal neutron-induced fission  
962 of  $^{233}\text{U}$  and  $^{235}\text{U}$ , but not for the spontaneous fission of  
963  $^{252}\text{Cf}$  or the neutron-induced fission of  $^{239}\text{Pu}$ . The promi-  
964 nence of this effect observed in the present work may be a

965 characteristic feature of the photofission of the even-even  
966  $^{238}\text{U}$  nucleus.

967 Interesting effects are also seen when plotting neutron  
968 correlation *versus* energy for several different opening an-  
969 gle cuts. Fig. 28 top shows the correlation when a min-  
970 imum threshold is applied to the absolute difference in  
971 the energies of coincident n-n pairs. Note that a sup-  
972 pression of correlated emission for large opening angles only  
973 occurs in n-n pairs that have a large difference in energy,  
974 as indicated by Fig. 28 top.

975 While a definitive explanation of these results would  
976 be greatly aided by detailed modeling studies, these data  
977 are consistent with two possible explanations relating to  
978 the unique feature of the asymmetric angular emission  
979 of fission fragments in photofission. First, the neutrons  
980 may indeed be emitted isotropically in the rest frame of  
981 the fission fragment, but one fragment essentially shad-  
982 ows the neutrons emitted from the other fragment, either  
983 through absorption or scattering, leading to a decrease in  
984 emission along the fission axis. The decrease in corre-  
985 lation at  $\theta_{nn}$ 's greater than  $170^\circ$  for n-n pairs with a large  
986 energy difference, as seen in Fig. 28 top, is consistent with  
987 the proposed shadowing mechanism for the case of neu-  
988 tron pairs emitted along the fission axis from the same

$^{252}\text{Cf}$  (SF)

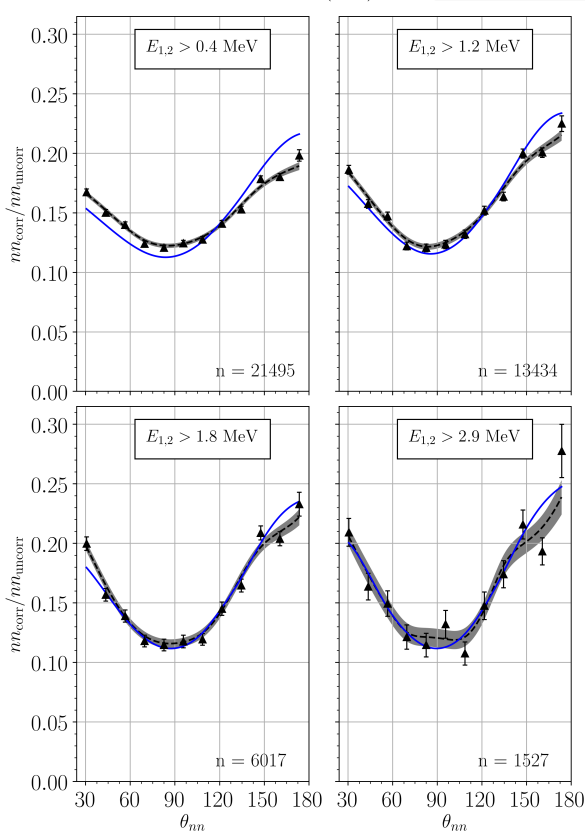


**FIG. 26:**  $\theta_{nn}$  distribution with minimum neutron energy cuts applied. The number of events contributing to each plot,  $n$ , is shown. Note that the lower right plots of this figure and Fig. 27 are identical.

$^{252}\text{Cf}$  (SF)

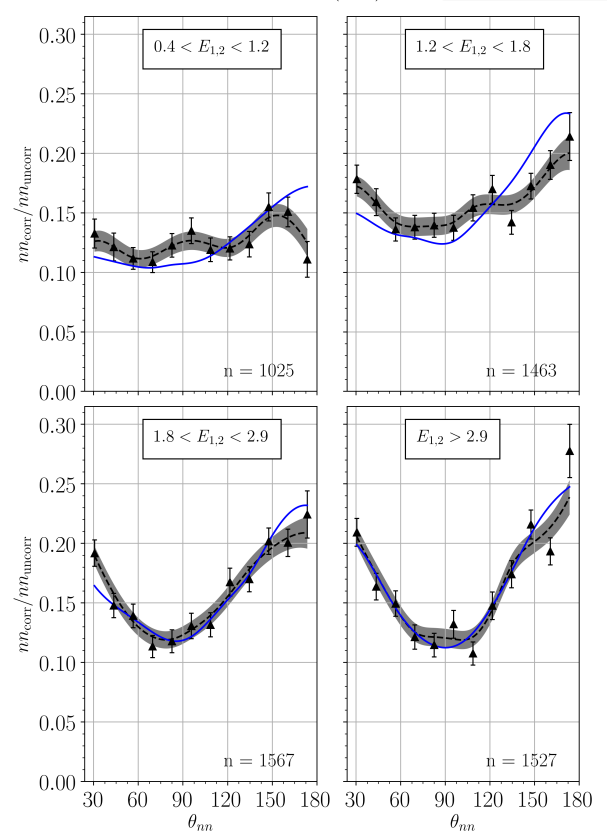


**FIG. 27:**  $\theta_{nn}$  distribution with cuts requiring that the energy of both coincident neutrons be within the specified range. The number of events contributing to each plot,  $n$ , is shown. Note that the lower right plots of this figure and Fig. 26 are identical.

989 fragment, because one neutron receives a boost to higher  
 990 energy from the fragment and the other a boost to lower  
 991 energy. The neutron boosted to lower energy is directed  
 992 toward the opposite fission fragment and is potentially  
 993 subject to interaction with it. On the other hand, Fig. 28  
 994 middle and bottom show no statistically significant de-  
 995 pendence in the correlation when maximum (middle) or  
 996 minimum (bottom) energy cuts are applied to each neu-  
 997 tron. To summarize the data, when both neutrons are  
 998 high energy and when both neutrons are low energy, there  
 999 does not seem to be an effect, but the effect is evident  
 1000 when there is a difference in energy. This is suggestive  
 1001 of a scenario whereby the decrease in correlation at large  
 1002 opening angles is associated with the emission of two neu-  
 1003 trons from the same fragment.

1004 A second possible explanation for this drop in n-n cor-  
 1005 relation at large opening angles is that there is, due to  
 1006 unknown reasons, a decrease in neutron emission along  
 1007 the fission axis. If it is the former case of shadowing, this  
 1008 effect has the potential to shed light on the time depen-

1009 dence of neutron emission, since shadowing would likely  
 1010 depend on the fission fragment separation. A definitive  
 1011 interpretation of this decreased n-n correlation for large  
 1012 opening angles in photofission requires further study.

### C. Considering $\theta_{abs}$

1014 As previously discussed in section IC, photofission dif-  
 1015 fers from spontaneous and neutron induced fission in that  
 1016 the fission fragments for the photon-induced reaction ex-  
 1017 hibit an asymmetry in their angle of emission, with the  
 1018 most likely orientation of the fission axis lying perpen-  
 1019 dicular to the direction of the incident photon. With  
 1020 this in mind, the following series of angular cuts were  
 1021 made on the data. Figure 29 shows the distributions of  
 1022 absolute angles of the n-n events for three different cuts  
 1023 on the value of the n-n opening angle. For n-n open-  
 1024 ing angles between  $120^\circ$  and  $160^\circ$ , there is an increased

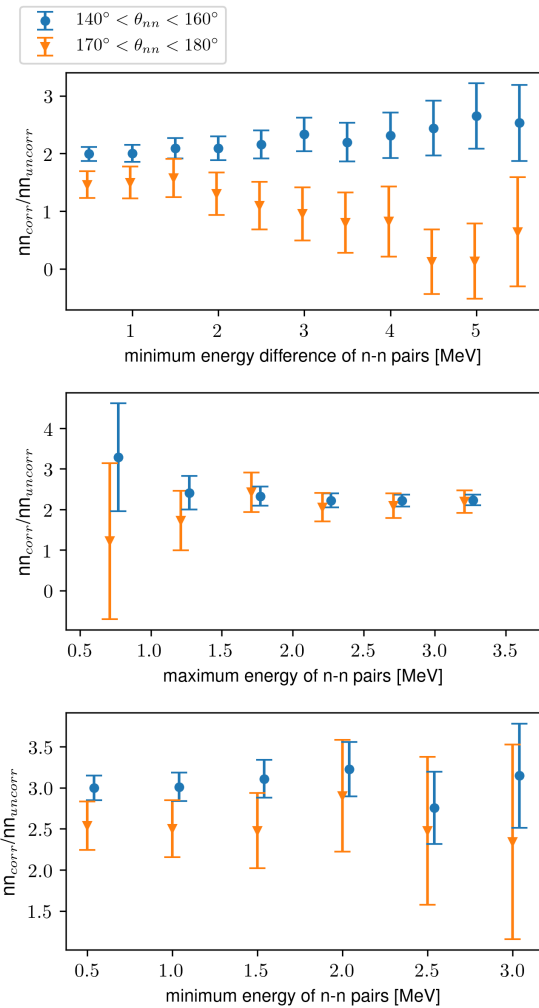


**FIG. 28:** From the photofission of  $^{238}\text{U}$ . The x-axes of each plot correspond to various cuts applied to the energies of the two neutrons forming coincident n-n pairs. (top) cuts are the minimum absolute difference between the energies of both coincident neutrons. (middle) cuts are a maximum energy threshold of both coincident neutrons, *i.e.* the left side of the plot corresponds to n-n pairs in which both neutrons have low energy. (bottom) cuts are a minimum energy threshold of both coincident neutrons, *i.e.* the right side of the plot corresponds to n-n pairs in which both neutrons have high energy.

1025 preponderance of both neutrons being emitted around  
1026  $90^\circ$ , consistent with the interpretation of kinematic fo-  
1027 cusing of neutrons coming from fission fragments which  
1028 are themselves being emitted preferentially at  $90^\circ$ . How-  
1029 ever, in the opening angle region where the n-n corre-  
1030 lation is reduced, from about  $160^\circ$  to  $180^\circ$ , this feature is  
1031 less prominent.

1032 Furthermore, if one plots the opening angle distribu-  
1033 tions for the case in which at least one neutron is emitted  
1034 perpendicular to the incident photon *versus* the case in  
1035 which neither neutron is emitted perpendicular to the  
1036 incident photon (Fig. 30), one sees distinct differences.

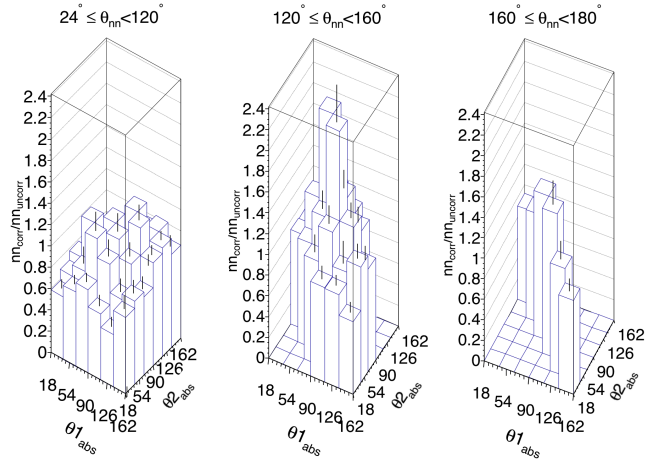


**FIG. 29:** Visualization of the correlation between the angles of each neutron with respect to the incident photon beam, denoted by  $\theta_{1\text{abs}}$  and  $\theta_{2\text{abs}}$ . Empty bins exist because of intrinsic geometrical phase-space. Data taken from measurements of  $^{238}\text{U}$  photofission.

1037 The fact that there are overall differences is not surpris-  
1038 ing, because in one case (Fig. 30 solid line) at least one  
1039 neutron preferentially receives a kinematic boost from a  
1040 fission fragment and in the other case (Fig. 30 dotted  
1041 line) neither neutron does. However, the fact that the  
1042 n-n correlation is reduced at  $180^\circ$  in opening angle when  
1043 at least one of the neutrons is emitted along the preferred  
1044 fission axis is unexpected. This is a feature which does  
1045 not seem to appear in most previous measurements of  
1046 either neutron-induced or spontaneous fission, as well as  
1047 our present measurement on spontaneous fission. The  
1048 attribution of this effect to the geometric coverage of the  
1049 neutron detection system or to neutron elastic scatter-  
1050 ing within the target was ruled out using simulations, as  
1051 discussed in section V C.

## VII. CONCLUDING REMARKS

1052 Neutron-neutron angular correlations in the photofis-  
1053 sion of  $^{238}\text{U}$  were measured using 10.5 MeV end-point  
1054 bremsstrahlung photons produced via a low duty factor,  
1055 pulsed linear electron accelerator. The measured angular  
1056 correlations reflect the underlying back-to-back nature of  
1057 the fission fragments. The method of analysis used a sin-  
1058 gle set of experimental data to produce an opening an-  
1059 gle distribution of correlated and uncorrelated neutron  
1060 pairs. A ratio is taken between these two sets to provide  
1061 a self-contained result of angular correlations, in that  
1062 the result is independent of neutron detector efficiencies.

1063 Neutron-neutron angular correlation measurements were  
1064 also made using neutrons from the spontaneous fission of  
1065  $^{252}\text{Cf}$  and show good agreement with previous measure-  
1066 ments.

1067 Measured n-n opening angle distributions from the  
1068 photofission of  $^{238}\text{U}$  are not in close agreement with the

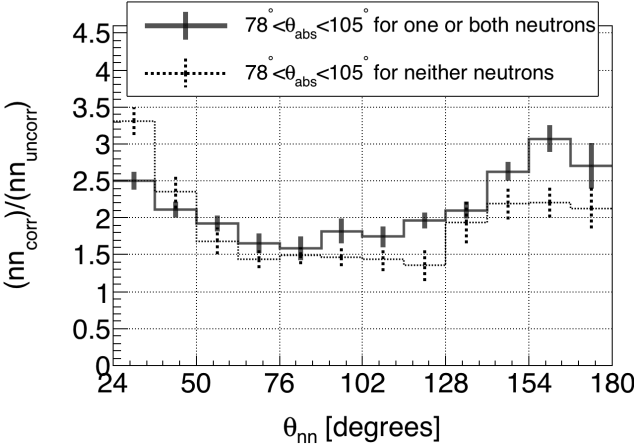


**FIG. 30:** Requiring that at least one of the coincident neutrons be emitted nearly perpendicular to the photon beam (solid line) produces an opening angle distribution that is different from that produced when it is required that both neutrons are emitted nearly parallel to the photon beam (dotted line). Data taken from measurements of  $^{238}\text{U}$  photofission.

ad hoc photofission model included in FREYA version 2.0.3. This is expected, because the model is only a crude approximation which uses a neutron-induced model to approximate photofission. The present measurement will be useful for fine-tuning photofission models included in future releases of FREYA.

In addition, we report for the first time a pronounced anomaly in the n-n angular distributions from photofission, in which the rate of neutron emission at opening angles near  $180^\circ$  is diminished, resulting in a local maximum at about  $160^\circ$  instead of the expected  $180^\circ$ . We offer two possible interpretations for this effect. First, the neutrons may indeed be emitted isotropically in the rest frame of the fission fragment, but one fragment essentially shadows the neutrons emitted from the other fragment, either through absorption or scattering. Second, that there is, due to unknown reasons, a decrease in neutron emission along the fission axis. While these measurements do not provide a definitive interpretation of this decreased n-n correlation for large opening angles in photofission, further study may have the potential to shed light on the time evolution of neutron emission in photofission.

It is our hope that these first measurements of n-n correlations in photofission will provide the impetus for future modeling of the fundamental physics of fission.

1096

## VIII. ACKNOWLEDGMENTS

This work has been supported by the National Nuclear Security Administration, grant DE-NA002488. We wish to thank the staff of the Idaho Accelerator Center for their assistance in this work. We also wish to acknowledge early contributions to this work by our friend and colleague the late David V. Jordan of the Pacific Northwest National Laboratory.

- 
- [1] J. T. Caldwell, E. J. Dowdy, R. A. Alvarez, B. L. Berman, and P. Meyer. Experimental determination of photofission neutron multiplicities for  $^{235}\text{U}$ ,  $^{236}\text{U}$ ,  $^{238}\text{U}$ , and  $^{232}\text{Th}$  using monoenergetic photons. *Nuclear Science and Engineering*, 73(2):153–163, 1980.
- [2] G. A. Petrov. Current status of the search for scission neutrons in fission and estimation of their main characteristics. *AIP Conference Proceedings*, 798(1):205–212, 2005.
- [3] Harry R. Bowman, Stanley G. Thompson, J. C. D. Milton, and Wladyslaw J. Swiatecki. Velocity and angular distributions of prompt neutrons from spontaneous fission of  $\text{Cf}^{252}$ . *Phys. Rev.*, 126:2120–2136, Jun 1962.
- [4] C. Budtz-Jørgensen and H.-H. Knitter. Simultaneous investigation of fission fragments and neutrons in  $^{252}\text{Cf}$  (SF). *Nuclear Physics A*, 490(2):307 – 328, 1988.
- [5] P. Talou, R. Vogt, J. Randrup, M. E. Rising, S. A. Pozzi, J. Verbeke, M. T. Andrews, S. D. Clarke, P. Jaffke, M. Jandel, T. Kawano, M. J. Marcath, K. Meierbachtol, L. Nakae, G. Rusev, A. Sood, I. Stetcu, and C. Walker. Correlated prompt fission data in transport simulations. *The European Physical Journal A*, 54(1):9, Jan 2018.
- [6] S. Debenedetti, J. E. Francis, W. M. Preston, and T. W. Bonner. Angular dependence of coincidences between fission neutrons. *Phys. Rev.*, 74:1645–1650, Dec 1948.
- [7] J. S. Pringle and F. D. Brooks. Angular correlation of neutrons from spontaneous fission of  $^{252}\text{Cf}$ . *Phys. Rev. Lett.*, 35:1563–1566, Dec 1975.
- [8] Sara A. Pozzi, Brian Wieger, Andreas Enqvist, Shaun D. Clarke, Marek Flaska, Matthew Marcath, Edward Larsen, Robert C. Haight, and Enrico Padovani. Correlated neutron emissions from  $^{252}\text{Cf}$ . *Nuclear Science and Engineering*, 178(2):250–260, 2014.
- [9] A. M. Gagarski, I. S. Guseva, V. E. Sokolov, G. V. Val'ski, G. A. Petrov, D. O. Krinitin, D. V. Nikolaev, T. A. Zavarukhina, and V. I. Petrova. Neutron-neutron angular correlations in spontaneous fission of  $^{252}\text{Cf}$ . *Bulletin of the Russian Academy of Sciences, Physics*, 72:773–777, July 2008.
- [10] J. M. Verbeke, L. F. Nakae, and R. Vogt. Neutron-neutron angular correlations in spontaneous fission of  $^{252}\text{Cf}$  and  $^{240}\text{Pu}$ . *Phys. Rev. C*, 97:044601, Apr 2018.
- [11] V. E. Sokolov and G. A. Petrov. Investigation of the angular dependences of neutron-neutron coincidences from  $^{252}\text{Cf}$ ,  $^{235}\text{U}$ ,  $^{233}\text{U}$  and  $^{239}\text{Pu}$  fission in search of scission neutrons. *Proc. XVIII Internat. Seminar on Interaction of Neutrons with Nuclei (ISSIN-18)*, pages 108–118, 2010.
- [12] Matthew J. Marcath, Tony H. Shin, Shaun D. Clarke, Paolo Peerani, and Sara A. Pozzi. Neutron angular distribution in plutonium-240 spontaneous fission. *Nuclear*

- 1154     *Instruments and Methods in Physics Research, Section 1174*  
 1155     *A: Accelerators, Spectrometers, Detectors and Associated 1175*  
 1156     *Equipment*, 830:163–169, 9 2016.  
 1157 [13] S Nair, D B Gayther, B H Patrick, and E M Bowey. 1176  
 1158     Fission-neutron and fragment angular distributions from 1178  
 1159     threshold photofission of  $^{232}\text{Th}$  and  $^{238}\text{U}$ . *Journal of 1179*  
 1160     *Physics G: Nuclear Physics*, 3(7):965, 1977.  
 1161 [14] J. M. Mueller, M. W. Ahmed, R. H. France, M. S. John- 1181  
 1162     son, H. J. Karwowski, L. S. Myers, J. Randrup, M. H. 1182  
 1163     Sikora, M. C. Spraker, S. Stave, J. R. Tompkins, R. Vogt, 1183  
 1164     H. R. Weller, C. S. Whisnant, and W. R. Zimmerman. 1184  
 1165     Prompt neutron polarization asymmetries in photofission 1185  
 1166     of  $^{232}\text{Th}$ ,  $^{233,235,238}\text{U}$ ,  $^{237}\text{Np}$ , and  $^{239,240}\text{Pu}$ . *Phys. Rev. 1186*  
 1167     *C*, 89:034615, Mar 2014.  
 1168 [15] Jefferson Lab. *CODA 2.6*, 2015.  
 1169 [16] Sara A Pozzi, Enrico Padovani, and Marzio Marseguerra. 1189  
 1170     MCNP-PoliMi: a Monte-Carlo code for correlation mea- 1190  
 1171     surements. *Nuclear Instruments and Methods in Physics 1191*  
 1172     *Research Section A: Accelerators, Spectrometers, Detec- 1192*  
 1173     *tors and Associated Equipment*, 513(3):550 – 558, 2003.  
 1193  
 1194 [17] Eric C. Miller, Shaun D. Clarke, Marek Flaska, Sara 1195  
 1196     A. Pozzi, and Enrico Padovani. MCNPX-PoliMi post-  
 1197     processing algorithm for detector response simulations.  
 1198     *JNMM, Journal of the Institute of Nuclear Materials 1199*  
 1200     *Management*, 40(2):34–41, 12 2012.  
 1201 [18] Lawrence Berkeley National LaboratoryLawrence Liver-  
 1202     more National LaboratoryLos Almost National Labora-  
 1203     toryUniversity of Michigan Nuclear Engineering. *FREYA 2.0.3*, 2016.  
 1204 [19] S. D. Clarke, B. M. Wieger, A. Enqvist, R. Vogt, J. Ran-  
 1205     drup, R. C. Haight, H. Y. Lee, B. A. Perdue, E. Kwan,  
 1206     C. Y. Wu, R. A. Henderson, and S. A. Pozzi. Mea-  
 1207     surement of the energy and multiplicity distributions of  
 1208     neutrons from the photofission of  $^{235}\text{U}$ . *Phys. Rev. C*,  
 1209     95:064612, Jun 2017.  
 1210 [20] Krishichayan, M. Bhike, A. P. Tonchev, and W. Tornow.  
 1211     Fission product yield measurements using monoenergetic  
 1212     photon beams. In *European Physical Journal Web of 1213*  
 1213     *Conferences*, volume 146 of *European Physical Journal 1214*  
 1214     *Web of Conferences*, page 04018, September 2017.  
 1215 [21] Kyle Cranmer. Kernel estimation in high-energy physics.  
 1216     *Computer Physics Communications*, 136(3):198–207,  
 1217     2001.